nature communications

Article

https://doi.org/10.1038/s41467-026-75292-2

Intracellular iron homeostasis-regulated epigenetic reprogramming contributes to −7/del(7q) leukemia

Received: 5 October 2025

Accepted: 25 June 2026

Published online: 10 July 2026

Check for updates

Jianan Zheng[1,8], Yiman Peng[1,8], Xintong Deng[1,8], Lanxin Zhang[1,8], Zhongwang Wang[2,8], Xuelan Chen[1], He Li[2], Yanxin Li[1], Qi Zhang[1], Liuxian Zheng[1], Ziyi Qi[1], Lan Wang[3], Min Lu[4], Wenguo Cui[5], Li Wang[4], Yu Wu[2], Weili Zhao[4], Ting Niu[2], Chong Chen[1,6,7] ✉ & Yu Liu[1,6,7] ✉

Chromosome copy number variations are poorly understood drivers of human malignancies. −7/del(7q) is common in acute myeloid leukemia, confers a poor prognosis, and is thought to harbor several tumor suppressors. Previously, we identified the histone methyltransferase *KMT2C* as a tumor suppressor in this region. Here, through a differentiation CRISPR screen in hematopoietic stem and progenitor cells, we find that the mitochondrial iron transporter ABCB8 is essential for their differentiation. *ABCB8* deficiency accelerates leukemogenesis in vivo and disrupts iron homeostasis, reducing cytoplasmic iron availability and impairing iron-dependent enzymes, including the histone demethylase KDM6A. Consequently, *ABCB8* loss elevates H3K27me3 levels, repressing differentiation genes in an iron- and KDM6A-dependent manner. Notably, *ABCB8* and *KMT2C*, neighboring genes on 7q, cooperatively regulate H3K27me3 to suppress leukemogenesis. Our findings reveal *ABCB8* as a tumor suppressor in −7/del(7q) acute myeloid leukemia and uncover an epigenetic collaboration between neighboring tumor suppressors, driven by iron-mediated chromatin remodeling.

Somatic copy number alterations (CNAs) are a hallmark of cancer[1,2] and occur as frequently as single-nucleotide variants (SNVs) in cancers. Recent work shows that over 70% of cancers harbor CNAs, with some lacking detectable driver SNVs altogether[3]. Unlike SNVs, which typically cause loss- or gain-of-function mutations in individual genes, CNAs often involve the amplification or deletion of larger chromosomal segments or even entire alleles. Examples include chromosome 17p deletions, monosomy 7, and 7q deletions[3–6]. These alterations can lead to the co-deletion or co-amplification of hundreds of genes. Cancers with such chromosomal CNAs are frequently associated with aggressive progression, drug resistance, and poor clinical outcomes[7,8]. For instance, acute myeloid leukemia (AML) with loss of chromosome 7 or del(7q) is classified as high-risk with an adverse prognosis[8,9]. Therefore, elucidating the molecular mechanisms by which CNAs drive

[1]Department of Hematology and Institute of Hematology, State Key Laboratory of Biotherapy and Cancer Center, West China Hospital, Sichuan University, Chengdu, China. [2]Department of Hematology and Institute of Hematology, West China Hospital, Sichuan University, Chengdu, China. [3]Shanghai Institute of Nutrition and Health, University of Chinese Academy of Sciences, Chinese Academy of Sciences, Shanghai, China. [4]Shanghai Institute of Hematology, State Key Laboratory of Medical Genomics, National Research Center for Translational Medicine at Shanghai, Ruijin Hospital Affiliated to Shanghai Jiao Tong University School of Medicine, Shanghai, China. [5]Department of Orthopaedics, Shanghai Key Laboratory for Prevention and Treatment of Bone and Joint Diseases, Shanghai Institute of Traumatology and Orthopaedics, Ruijin Hospital, Shanghai Jiao Tong University School of Medicine, 197 Ruijin 2nd Road, Shanghai, China. [6]State Key Laboratory of Biotherapy and Cancer Center, West China Hospital, Sichuan University, Chengdu, China. [7]Frontiers Medical Center, Tianfu Jincheng Laboratory, Chengdu, Sichuan, China. [8]These authors contributed equally: Jianan Zheng, Yiman Peng, Xintong Deng, Lanxin Zhang, Zhongwang Wang. ✉e-mail: chongchen@scu.edu.cn; yuliuscu@scu.edu.cn

tumor initiation and progression is crucial for advancing cancer research and therapy.

Studies from multiple groups have demonstrated that frequently deleted chromosomal regions are enriched in tumor suppressor genes (TSGs)[7,10–12]. For example, several TSGs, including *EIF5A*, *PHF23*, and *ALOX15B*, were recently identified on chromosome 17p, one of the most commonly deleted regions in human cancers and home to the well-known tumor suppressor gene *TP53*[7,13–15]. These studies not only highlight the complexity of the mechanisms by which chromosome 17p deletions promote tumor formation but also uncover tumor suppressive networks in cancers, such as the polyamine-hypusine axis, the *PHF23-SIN3-HDAC* epigenetic regulatory pathway, and arachidonic acid metabolism reprogramming.

Interestingly, TSGs located in these deleted chromosomal regions often exhibit rare mutations in cancers. Additionally, some TSGs, such as *KMT2C* on chromosome 7q36, drive tumorigenesis only when their mRNA levels are reduced by half, suggesting that the remaining wild-type allele is essential for tumor cell growth[16]. Given that hundreds of genes undergo copy number changes with chromosomal deletions, their collective impact on cancer biology remains underexplored. Further research into these mechanisms is critical for advancing our understanding of cancer progression and identifying potential therapeutic targets.

Here, we report the identification of *ABCB8* as a tumor suppressor gene on chromosome 7q36. Loss of *ABCB8* inhibits the differentiation of hematopoietic stem and progenitor cells (HSPCs) and promotes AML development in mouse models, similar to *KMT2C* chromosome 7 loss or 7q deletions, which are frequently observed in myelodysplastic syndrome (MDS) and AML and are often associated with poor prognosis[17–19]. *ABCB8* encodes an ATP-binding cassette subfamily B member 8, which is involved in mitochondrial iron transport. Mechanistically, the tumor-suppressive function of ABCB8 is linked to epigenetic reprogramming, likely through its impact on the iron-binding histone demethylase KDM6A. This results in increased trimethylation of lysine 27 on histone H3 (H3K27me3), a key epigenetic mark. Our findings uncover a critical iron-epigenetic regulatory network mediated by the ABCB8-KDM6A axis, highlighting its essential role in cancer biology.

Results

Abcb8 loss prevents HSPCs differentiation

By analyzing the samples from The Cancer Genome Atlas (TCGA)-LAML[20] samples, we found that 67 genes, in addition to *KMT2C*, are highly frequent co-deletions. Among them, 55 are conserved in the mouse genome. Considering that heterozygous deletion of *KMT2C* or chromosome 7q leads to a differentiation block in hematopoietic stem and progenitor cells (HSPCs)[16,21], we evaluated the individual impact of these 55 genes on HSPCs differentiation. This was measured by flow cytometry analysis of the differentiation markers Gr-1 and CD11b in c-Kit$^+$ HSPCs isolated from murine bone marrow (Fig. 1A, Supplementary Data 1). As shown in Fig. 1B, C, two sgRNAs targeting *Abcb8* were found to induce a dramatic decrease in the percentage of CD11b$^+$ or Gr-1$^+$ differentiated cells, compared to sgScr controls (Fig. 1B, C, Supplementary Fig. 1A). A similar differentiation blockade in HSPCs was observed with *Abcb8* shRNA (Fig. 1D, Supplementary Fig. 1B), supporting that *Abcb8* plays a role in hematopoiesis. We further analyzed the transcriptomics of mouse HSPCs (c-Kit$^+$) with *Abcb8* or control shRNA. Compared to the control sh*Ren* group, genes involved in various differentiation pathways like lymphocyte differentiation, regulation of leukocyte differentiation, and regulation of hematopoiesis were significantly decreased in sh*Abcb8* HSPCs (Fig. 1E). Gene set enrichment analysis (GSEA) also showed that WP_HEMATOPOIETIC_STEM_CELL_DIFFERENTIATION and KEGG_HEMATOPOIETIC_CELL_LINEAGE gene sets were significantly enriched in control sh*Ren* group (NES = −2.05 and −2.10; *p.adj* < 0.01 and <0.01, respectively; Fig. 1F). Together, these results suggest that loss of *Abcb8* impairs hematopoietic differentiation.

Interestingly, from scRNA-seq analysis of bone marrow from 25 healthy human donors[22], we found that *ABCB8* is mainly expressed in HSPCs and progenitor cells (GMP and MEP), with mRNA levels dramatically decreasing in mature myeloid cells (Fig. 1G, H, Supplementary Fig. 1C). Also, CytoTRACE[23], a computational method to predict undifferentiation states of cells according to their scRNA-seq data, was applied to analyze the correlation between *ABCB8* expression and cell differentiation. The result shows that *ABCB8* is positively correlated with CytoTRACE scores along the HSPC-GMP-monocyte differentiation axis (Fig. 1I). Moreover, we sorted mouse LSK (Lin$^-$Sca-1$^+$c-Kit$^+$), CMP (Lin$^-$Sca-1$^-$c-Kit$^+$CD34$^+$CD16/32$^-$), GMP (Lin$^-$Sca-1$^-$c-Kit$^+$CD34$^+$CD16/32$^+$), MEP (Lin$^-$Sca-1$^-$c-Kit$^+$CD34$^-$CD16/32$^-$), macrophage (CD11b$^+$), and granulocyte (Gr-1$^+$) cells (Fig. 1J) out of bone marrow, and measured the *Abcb8* expression by RT-qPCR. As Fig. 1J shows, *Abcb8* mRNA levels are much higher in progenitor cells (LSK, CMP, GMP and MEP) than in more mature cells (CD11b$^+$ or Gr-1$^+$ cells). Together, these results suggest a role for *Abcb8* in the differentiation of hematopoietic stem and progenitor cells into myeloid cells.

To explore the hematopoietic phenotypes of *Abcb8* deficiency in vivo, we performed a competitive bone marrow transplantation assay. As Fig. 1K shows, CD45.1 wild-type c-Kit$^+$ HSPCs were transduced with GFP-linked shRNAs (sh*Abcb8* #1, #2 or control sh*Ren*), followed by transplantation into irradiated CD45.2 recipients. Peripheral blood analysis from recipient mice showed that the percentage of GFP$^+$ cells in the sh*Abcb8* CD45.1 population was progressively reduced compared to that in the sh*Ren* cohort at 6 and 8 weeks after transplantation (Fig. 1L). Of note, myeloid cells (CD11b$^+$ or Gr-1$^+$) in GFP$^+$ cells were decreased in the sh*Abcb8* group at 6 and 8 weeks post-transplantation (Supplementary Fig. 1D).

We harvested bone marrow from recipient mice at 8 weeks post-transplantation. Although GFP$^+$ cell numbers in sh*Abcb8* groups were reduced in bone marrow (Supplementary Fig. 1E), the percentage of LSK (Lin$^-$Sca-1$^+$c-Kit$^+$) stem/progenitor cells within the GFP$^+$ population was increased (Fig. 1M). Further flow cytometry analysis of LSK subpopulations showed increased proportions of short-term hematopoietic stem cells (ST-HSC, Lin$^-$Sca-1$^+$c-Kit$^+$CD48$^+$CD150$^+$) and long-term hematopoietic stem cells (LT-HSC, Lin$^-$Sca-1$^+$c-Kit$^+$CD48$^-$CD150$^+$) while decreased proportions of multipotent progenitor cells (MPP, Lin$^-$Sca-1$^+$c-Kit$^+$CD48$^+$CD150$^-$) in the sh*Abcb8* group compared to the control sh*Ren* ones (Fig. 1N). These results indicate a myeloid differentiation block induced by *Abcb8* KD alone, suggesting that it may have the potential to develop MDS-like features.

Abcb8 deficiency drives leukemia formation

To investigate the role of *ABCB8* in leukemogenesis, we first analyzed *ABCB8* status in leukemia patients. Stratifying the TCGA-LAML patient cohort by the change in the copy number of *ABCB8* demonstrated a shorter overall survival in patients whose leukemias carried *ABCB8* deletions (Fig. 2A). Leukemia cells with *ABCB8* deletions have a significant reduction of the *ABCB8* mRNA level compared to those with intact *ABCB8* (Fig. 2B). Given that *ABCB8* is often co-deleted with other genes like *KMT2C* in chromosome 7q deletions, we analyzed the impact of *ABCB8* expression level on survival by using the maximally selected rank statistics (maxstat) method, as implemented in the survminer package[24]. The results showed that low *ABCB8* expression level is associated with a poor prognosis in multiple cohorts, including the Beat AML[25], GSE146173[26] and GSE37642[27] (Supplementary Fig. 2A–E). Of note, the expressions of other genes close to *ABCB8*, like *KMT2C* or *EZH2*, are not decreased in the *ABCB8* low cohorts, indicating that lower *ABCB8* expression may be a poor prognosis indicator (Supplementary Fig. 2C, E). Interestingly, *ABCB8* has rare single-nucleotide variants from the analysis of TCGA-LAML data, and is frequently co-deleted with *TP53* and *NF1* (Supplementary Fig. 2F).

https://doi.org/10.1038/s41467-026-75292-2

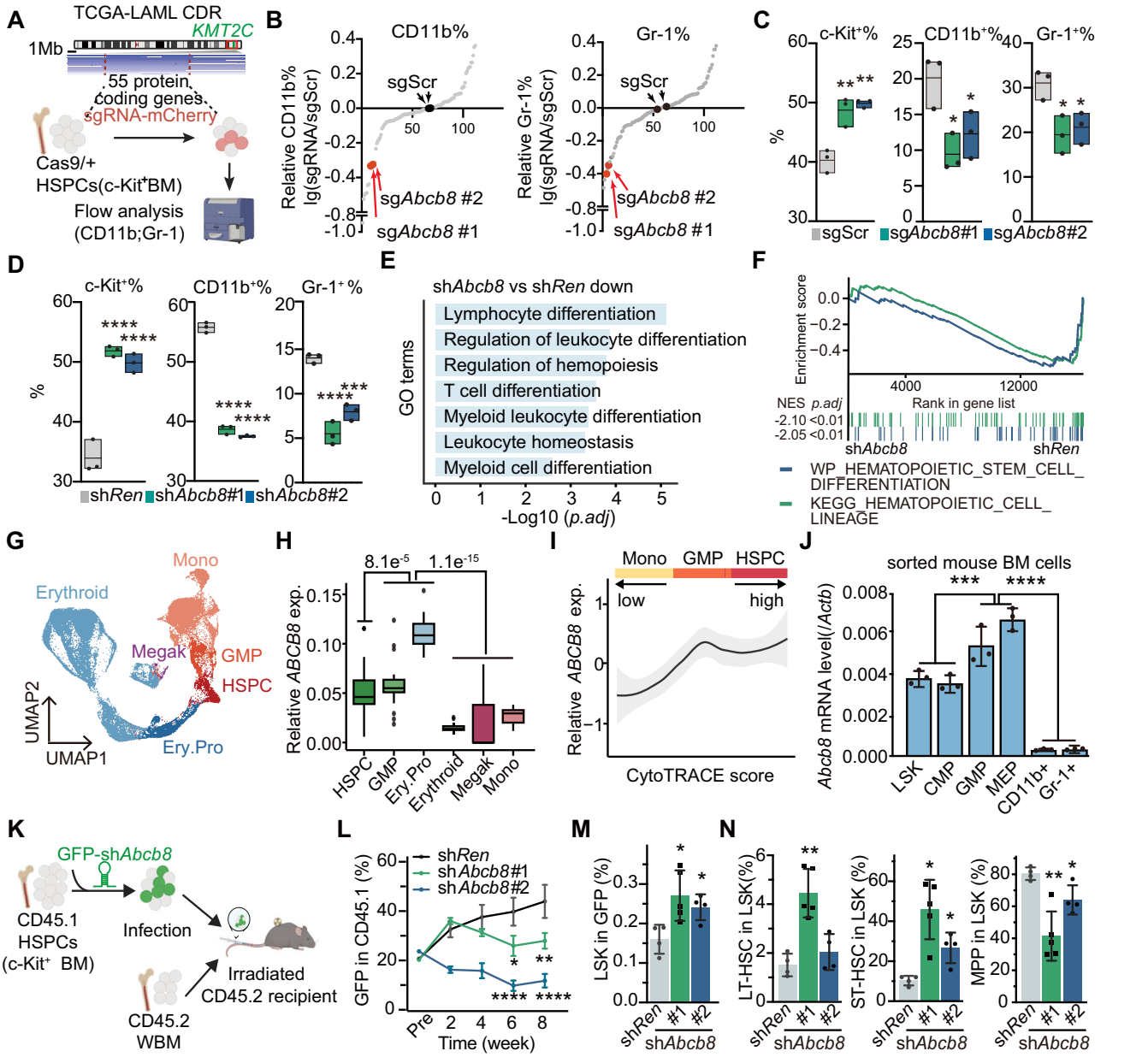


Fig. 1 | *Abcb8* loss prevents HSPCs differentiation. A Schematic of the CRISPR/Cas9 screening strategy to identify 7q CDR genes whose loss blocks HSPC differentiation. **B** Scatter plot showing the relative levels of CD11b% or Gr-1% in c-Kit$^+$ BM cells infected with sgRNAs or control sgScr. **C**, **D** Bar graphs depicting the percentages of c-Kit$^+$, CD11b$^+$, and Gr-1$^+$ cells in c-Kit$^+$ BM cells with sg*Abcb8* or sgScr (**C**), sh*Abcb8* or sh*Ren* (**D**). $n = 3$ biological repeats, center denoted by the median, lower and upper bounds defined the minimum and maximum. **E**, **F** GO enrichment analysis (**E**) and GSEA (**F**) of downregulated pathways in sh*Abcb8* c-Kit$^+$ BM cells ($n = 6$ biological repeats), compared to sh*Ren* control cells ($n = 3$ biological repeats). **G** The UMAP plot of scRNA-seq analysis of healthy human BM cells[22]. $n = 37186$ cells from 25 samples in (**G**, **H**). **H** Pseudo-bulk averages of log-normalized *ABCB8* expression across healthy human BM cell types[22]. Box plots show the median, 25th–75th percentiles, and whiskers extending to 1.5 × IQR. **I** Correlation between z-scored *ABCB8* expression and CytoTRACE scores in Mono, GMP and HSPC cells ($n = 14012$ cells from 25 samples), lower CytoTRACE score indicates more differentiated cells. The gray shaded band indicates the 95% confidence interval around the LOESS-fitted curve. **J** RT-qPCR results of *Abcb8* mRNA levels relative to *Actb* in mouse hematopoietic subsets. $n = 3$ mice. **K** Schematic of competitive BM transplantation. **L** Percentage of GFP$^+$/CD45.1$^+$ cells in the peripheral blood of the recipient mice. $n = 7$ mice/cohort. **M** Percentage of LSK (Lin$^-$ Sca1$^+$ c-Kit$^+$) cells within the GFP$^+$ BM at 11 weeks post-transplantation. **N** Percentage of LT-HSC, ST-HSC, and MPP in LSK at 11 weeks post-transplantation. **M**, **N**: sh*Ren* $n = 4$; sh*Abcb8* #1 $n = 5$, sh*Abcb8* #2 $n = 4$ mice. $^*p < 0.05$, $^{**}p < 0.01$, $^{***}p < 0.001$, $^{****}p < 0.0001$. A and K, Created in BioRender. Pang, X. (2026) https://BioRender.com/185na5c. Data are presented as mean ± SEM (**L**) or mean ± SD (**J**, **M**, **N**). Statistical significance was assessed by two-tailed one-way ANOVA with Dunnett's test (**C**, **D**, **M**, **N**), two-tailed two-way ANOVA with Dunnett's test (**L**), one-sided hypergeometric test with Benjamini-Hochberg adjustment (**E**), permutation-based *p*-values with Benjamini-Hochberg adjustment (**F**) or two-tailed unpaired *t*-test (**H**, **J**). Source data are provided as a source data file.

Consistent with our previous results that *ABCB8* loss induces HSPCs differentiation block, analysis of the transcriptomics from the Beat AML cohort showed that lower leukemia *ABCB8* expression had significantly reduced enrichment of genes involved in several differentiation-related pathways, like hematopoietic cell lineage and myeloid differentiation pathway (Fig. 2C). Gene set enrichment analysis has similar results. The POSITIVE_REGULATION_OF_STEM_CELL_DIFFERENTIATION and STEM_CELL_DIFFERENTIATION

https://doi.org/10.1038/s41467-026-75292-2

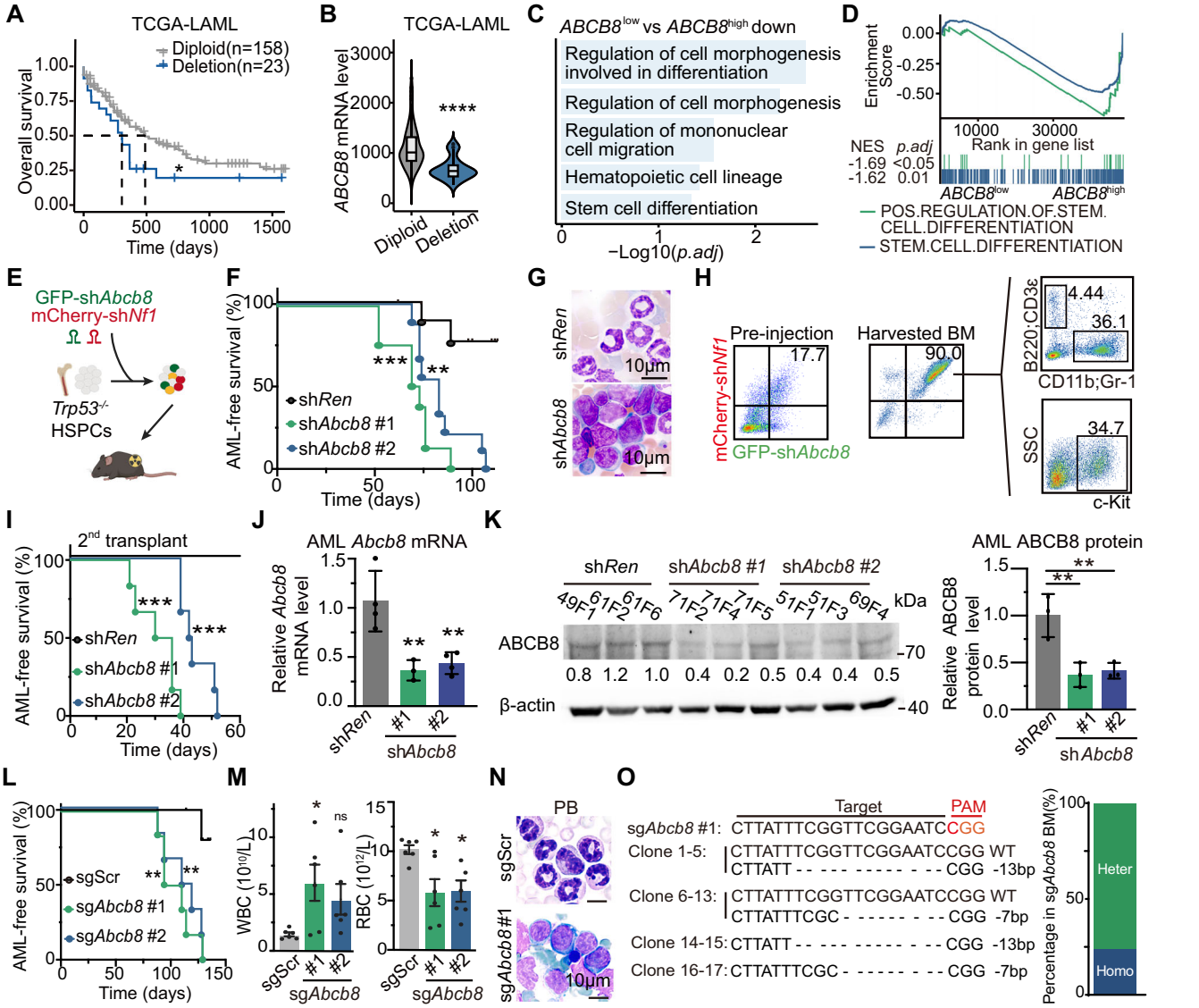


Fig. 2 | *Abcb8* deficiency drives AML. A Kaplan-Meier survival of AML patients with *ABCB8* diploid ($n = 158$) or deletion ($n = 23$) from TCGA-LAML[20] cohort, log-rank test. **B** DESeq2-normalized relative *ABCB8* expression in AML patients with Diploid ($n = 123$) or Deletion ($n = 21$) of *ABCB8* (TCGA-LAML[20]). Box plots show the median, 25th-75th percentiles, and 1.5 × IQR whiskers. **C**, **D** GO and KEGG enrichment analysis (**C**) and GSEA(**D**) of *ABCB8*-low ($n = 32$) vs. *ABCB8*-high ($n = 617$) BeatAML patients[25]. GO/KEGG used downregulated genes in *ABCB8*-low ($\log_2FC < -1$, $p < 0.05$). **E** Schematic of TNA (*Trp53*$^{-/-}$; sh*Nf1*; sh*Abcb8*) AML models generation. Created in BioRender. Pang, X. (2026) https://BioRender.com/185na5c. **F** Kaplan-Meier survival curves of recipients in sh*Ren* ($n = 11$ mice), sh*Abcb8* #1($n = 8$ mice) or sh*Abcb8* #2 ($n = 9$ mice) cohort. Log-rank test. **G** Wright-Giemsa-stained peripheral blood from sh*Ren* or sh*Abcb8* cohort. Scale bar, 10 μm. **H** Flow cytometry of pre-transplant donor cells and recipient BM leukemia cells from the sh*Ren* or sh*Abcb8* cohort. **I** Kaplan-Meier survival curves of 2nd transplant recipient mice (2 donors/cohort, 3 recipients/donor, $n = 6$ mice/cohort, median survival, sh*Ren* not reached, #1 42.5 days, #2 33 days, log-rank test). **J** RT-qPCR results of *Abcb8* mRNA levels in sh*Ren*, sh*Abcb8* recipient mouse BM ($n = 3$ mice). **K** Protein levels of ABCB8 (left) and quantification (right) in sh*Ren*, sh*Abcb8* recipient mouse BM ($n = 3$ mice). **L** Kaplan-Meier AML-free survival of recipient mice in sgScr or sg*Abcb8* cohort ($n = 6$ mice/cohort, log-rank test). **M** WBC and RBC counts in sgScr or sg*Abcb8* cohort at 10 weeks or at death if earlier ($n = 6$ mice/cohort). **N** Wright-Giemsa-stained peripheral blood from sgScr or sg*Abcb8* cohort. Scale bar,10 μm. **O** Sequences of sg*Abcb8* #1 targeted region in recipient BM cells ($n = 17$ independent clones). The bar chart shows genotypic distribution. $^*p < 0.05$, $^{**}p < 0.01$, $^{***}p < 0.001$, $^{****}p < 0.0001$. Data are presented as mean ± SD (**J**, **K**, **M**). Statistical significance was assessed by one-sided hypergeometric test with Benjamini-Hochberg adjustment (**C**), permutation-based *p*-values with Benjamini-Hochberg adjustment (**D**) or two-tailed unpaired *t*-test (**B**). **G**, **H**, **N** are representative images of 6 mice. Source data are provided as a source data file.

gene sets were significantly negatively enriched in *ABCB8*^{low} AML samples (NES = −1.69 and −1.62; *p.adj* < 0.05 and = 0.01, respectively; Fig. 2D).

We further investigated whether *Abcb8* loss promoted leukemogenesis with a mouse transplantation-based leukemia model. Given the co-occurrence of *ABCB8* deletions with *TP53* and *NF1* alterations in TCGA-LAML (Supplementary Fig. 2F), we introduced sh*Abcb8* or control sh*Ren*, combined with sh*Nf1*, into *Trp53*$^{-/-}$ mouse bone marrow-derived c-Kit$^+$ HSPCs, followed by transplantation into sub-lethally irradiated wild-type B6 recipient mice (Fig. 2E). Recipient mice were monitored regularly. After 10 weeks post-transplantation, mice in the sh*Abcb8* cohort displayed significantly increased peripheral white blood cell (WBC) counts compared to the control sh*Ren* cohort, along with variably decreased hemoglobin (Hb) and platelet (PLT) levels, indicative of leukemic expansion and suppression of normal hematopoiesis (Supplementary Fig. 2G). Consequently, the sh*Abcb8* cohort had a significantly shorter AML-free survival (median onset 71 days for sh*Abcb8* #1, 83 days for sh*Abcb8* #2), while only two of nine mice in the

sh*Ren* cohort developed AML (Fig. 2F). The other sh*Ren* mice developed myeloproliferative neoplasm, as shown by more mature myeloid cells instead of blast cells in peripheral blood smear (Fig. 2G). Flow cytometry revealed that GFP-linked sh*Abcb8* was enriched in leukemia cells, suggesting a selective advantage for *Abcb8*-deficient cells during leukemia progression. All recipients with *Abcb8* knockdown developed AML, partially expressed c-Kit and CD11b/Gr-1 (Fig. 2H). Compared to the sh*Ren* cohort, recipient mice transplanted with sh*Abcb8* developed aggressive acute myeloid leukemia as shown by sh*Abcb8*$^+$ blasts enriched in PB (Fig. 2G), severe leukemia cell infiltration into spleen and liver (Supplementary Fig. 2H), and the ability to generate AML in second transplanted wild-type recipient mice (Fig. 2I). The *Abcb8* mRNA levels in the harvested leukemia cells were reduced (Fig. 2J), and ABCB8 protein levels were decreased by approximately half (Fig. 2K). Similarly, genes downregulated in 7q deleted human AMLs compared to those without 7q deletions were significantly negatively enriched in sh*Ren* HSPCs relative to sh*Abcb8* HSPCs (NES = −1.50, p-value < 0.01) (Supplementary Fig. 2I).

We also investigated the ABCB8 impact on leukemia genesis with CRISPR/Cas9 (Supplementary Fig. 2J). Consistently, *Abcb8* sgRNAs, together with sh*Nf1*; *Trp53*$^{-/-}$, promoted leukemia formation in recipient mice (median onset: 102 days for sg*Abcb8* #1); 114 days for sg*Abcb8* #2) while only one of six control sgScr recipient mice developed leukemia during the observation period (Fig. 2L). Similar to the sh*Abcb8* cohort, recipient mice transplanted with sg*Abcb8* HSPCs developed AML, as shown by WBC, red blood cell (RBC), CD11b$^+$/Gr-1$^+$; c-Kit$^+$ (Fig. 2M, Supplementary Fig. 2K), blasts in blood smear (Fig. 2N), leukemia infiltration in spleen, liver, and bone marrow (Supplementary Fig. 2L). Similarly, compared to the sgScr cohort, mice receiving sg*Abcb8*-transduced tumor cells exhibited more aggressive leukemia, indicated by accelerated leukemogenesis upon secondary transplantation (Supplementary Fig. 2M). Moreover, we examined the *Abcb8* mutation status in harvested bone marrow from the sg*Abcb8* AML cohort. As shown in Fig. 2O, 17 out of 20 individually picked sg*Abcb8* bone marrow cells exhibited loss-of-function mutations in *Abcb8*. Of note, 75% of the mutated cells were heterozygous, with the other *Abcb8* allele remaining wild-type, supporting a haploinsufficient tumor suppressor effect of *Abcb8*.

ABCB8 loss leads to nuclear iron deficiency, contributing to HSPCs differentiation

ABCB8 belongs to the ABC transporter family. It is located on the mitochondrial membrane, in charge of pumping mitochondrial iron and Fe-S out to the cytoplasm. It has been reported that *Abcb8* loss led to the accumulation of mitochondrial ferrous ions (Fe^{2+}) in cardiac tissue[28]. We observed the accumulation of iron in mitochondria in sg*Abcb8*-infected murine myeloid progenitor 32D cell line, as detected by a mitochondria-specific fluorescent dye FerroGreen (Supplementary Fig. 3A). Similar results were observed in the human HL-60 cell line carrying sg*ABCB8* (Supplementary Fig. 3B, C). Of note, the nuclear Fe^{2+} level was reduced in HL-60 cells infected with sg*ABCB8* when another iron dye, FerroOrange, was used (Fig. 3A–C). These results were confirmed with the ferrozine assay[29,30], measuring non-heme iron level in isolated mitochondrial and nuclear proteins (Fig. 3D, Supplementary Fig. 3D). Following *ABCB8* knockout, mitochondrial ferrous iron (Fe^{2+}) levels were significantly increased, while nuclear ferrous iron was markedly decreased (Fig. 3E). Given Fe^{2+} is an important cofactor for DNA and histone demethylases[31,32], we proposed that ABCB8 loss may cause epigenetic reprogramming that contributes to *Abcb8* deletion-driven HSPCs differentiation block and transformation. To investigate it, we first treated HSPCs carrying sh*Abcb8* or sh*Ren* with ferrous ammonium sulfate (FAS) to increase the Fe^{2+} level. Flow cytometry analysis showed that although iron supplementary treatment has little effect on freshly isolated murine c-Kit$^+$ HSPCs with control sh*Ren*, it significantly rescued the differentiation block induced by sh*Abcb8* compared to control sh*Ren*, as shown by reduced stemness marker c-Kit$^+$% and increased mature cell surface marker Gr-1$^+$%. This phenotype can be inhibited when the ferrous ion chelator deferiprone (DFP) is added together with FAS (Fig. 3F). Similar results were observed in leukemia cells. DFP treatment effectively repressed the effect of exogenous *ABCB8* on promoting the differentiation of the *Abcb8*-deficient leukemia cells (Fig. 3J).

Meanwhile, we sorted murine sh*Ren* or sh*Abcb8* c-Kit$^+$ cells treated with vehicle DMSO or FAS, followed by RNA sequencing (RNA-seq) analysis (Supplementary Fig. 3E). GO analysis shows several differentiation-related pathways were upregulated in FAS-treated cells (Fig. 3G). Furthermore, genes that were downregulated in sh*Abcb8* cells compared to sh*Ren* under vehicle treatment were upregulated when sh*Abcb8* cells were treated with FAS (Fig. 3H, I, Supplementary Data 3). Altogether, these results support that ABCB8 regulates the cell fate of HSPCs mainly through controlling the nuclear Fe^{2+} level.

ABCB8 deficiency upregulates histone H3 lysine27 methylation levels

Fe^{2+} is known to be a cofactor for nuclear demethylases. Therefore, we have measured various histone methylation levels and found that H3K27me3 levels were dramatically increased in *Abcb8*-deficient murine leukemic cells (Fig. 4A, Supplementary Fig. 4A). Compared to control sh*Ren* cells, sh*Abcb8*-driven AML cells had increased H3K27me3 levels (Fig. 4B). Exogenous *ABCB8* expression in sh*Abcb8* AML cells caused the reduction of H3K27me3 (Fig. 4C). Consistently, sg*Abcb8* in murine myeloid progenitor cell line 32D cells increased H3K27me3 levels (Fig. 4D).

We assessed the impact of sh*Abcb8* on H3K27me3 using the CUT&Tag sequencing in sorted c-Kit$^+$CD11b$^-$Gr-1$^-$ HSPCs. Consistent with global H3K27me3 protein level enhanced in *Abcb8*-deficient cells, the H3K27me3-bound peaks were generally increased (16034 peaks up, $Log_2FC > 1.5$, $p < 0.05$) in sh*Abcb8* HSPCs, compared to those in sh*Ren* controls (Fig. 4E, F, Supplementary Data 4). The increased peaks were predominantly enriched in gene promoter and intergenic regions (Supplementary Fig. 4B). This increase of H3K27me3-bound peaks was more dramatic for the genes whose expression was reduced by sh*Abcb8* (Fig. 4G, H). GO and Gene set enrichment analysis showed that H3K27me3 levels of genes enriched in GOBP_STEM_CELL_DIFFERENTIATION and GOBP_REGULATION_OF_MYELOID_CELL DIFFERENTIATION pathways, including *Cebpa, Gfi1,* were significantly upregulated in sh*Abcb8* samples (NES = 1.23 and 1.13; p-value < 0.01 and = 0.01, respectively; Fig. 4I–K).

We measured the H3K27me3 protein level in 32D, U937, or mouse c-Kit$^+$ CD11b$^-$Gr-1$^-$ HSPCs treated with DFP or FAS, and found that DFP increased H3K27me3 levels, an effect that was rescued by supplementation with FAS (Fig. 4L, M, Supplementary Fig. 4C). Moreover, we have performed the CUT&Tag sequencing for H3K27me3 in the murine c-Kit$^+$CD11b$^-$Gr-1$^-$ HSPCs treated with DMSO, DFP only, or DFP and FAS. H3K27me3 levels are elevated in cells treated with DFP, and back to similar levels as those in the DMSO group when combined with DFP and FAS treatment(Fig. 4N, O). Genes significantly upregulated by DFP vs DMSO but downregulated by DFP + FAS vs DFP were enriched in myeloid differentiation-related pathways (Fig. 4P, Q, Supplementary Data 4). These results supported that ABCB8 deficiency regulates histone methylation through ferrous iron.

ABCB8 loss deteriorates iron-dependent KDM6A function

Histone demethylase KDM6A is known as a critical demethylase for H3K27me3. *KDM6A* alterations, which frequently happen in AML, have been demonstrated to promote leukemia formation through inducing the differentiation block of HSPCs[33,34]. Among the genes that showed significantly higher H3K27me3 modification signals in sh*Abcb8* c-Kit$^+$CD11b$^-$Gr-1$^-$HSPCs, 56.7% exhibited KDM6A binding, based on the published KDM6A ChIP-seq data[34] from mouse HSPCs (Fig. 5A).

https://doi.org/10.1038/s41467-026-75292-2

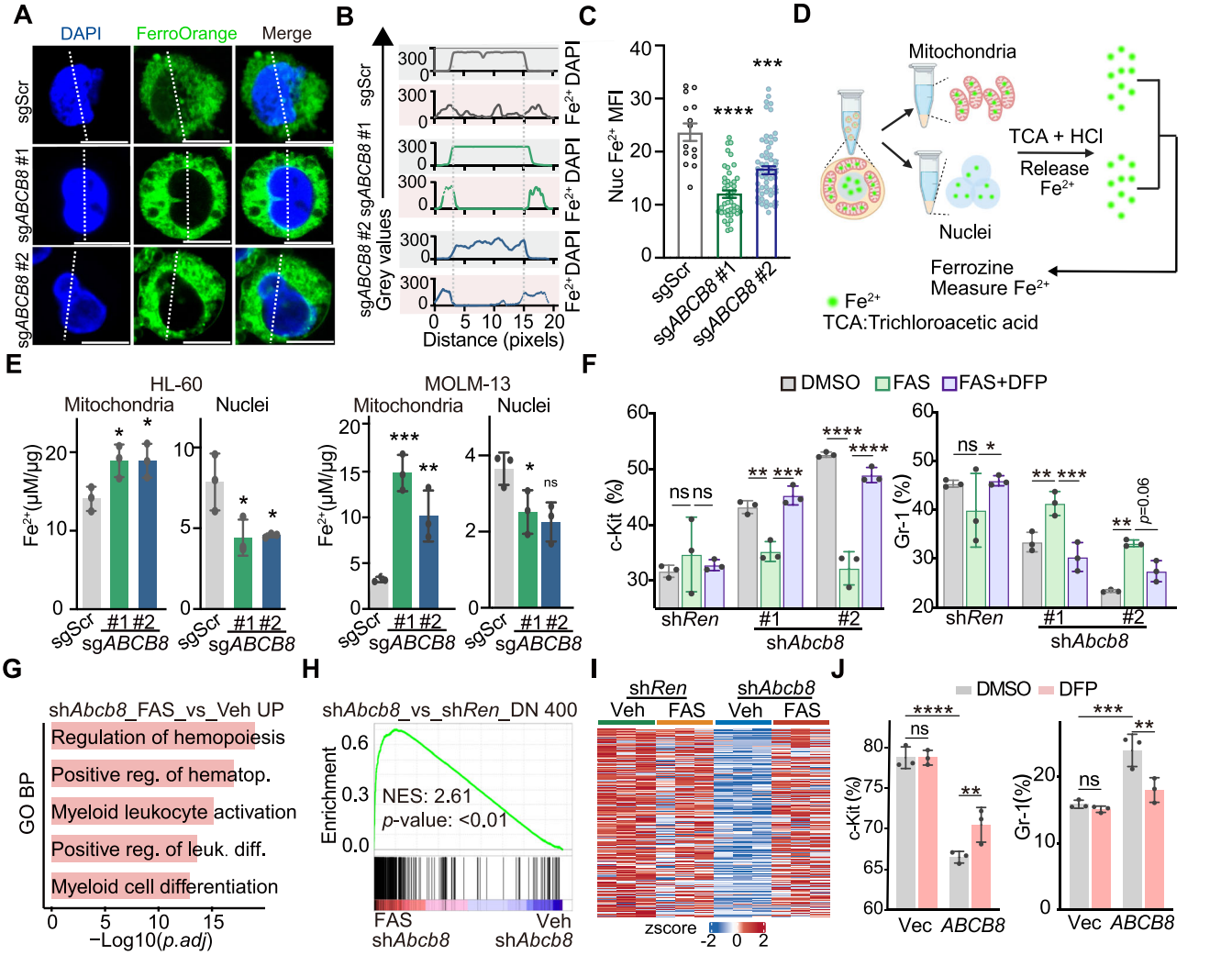
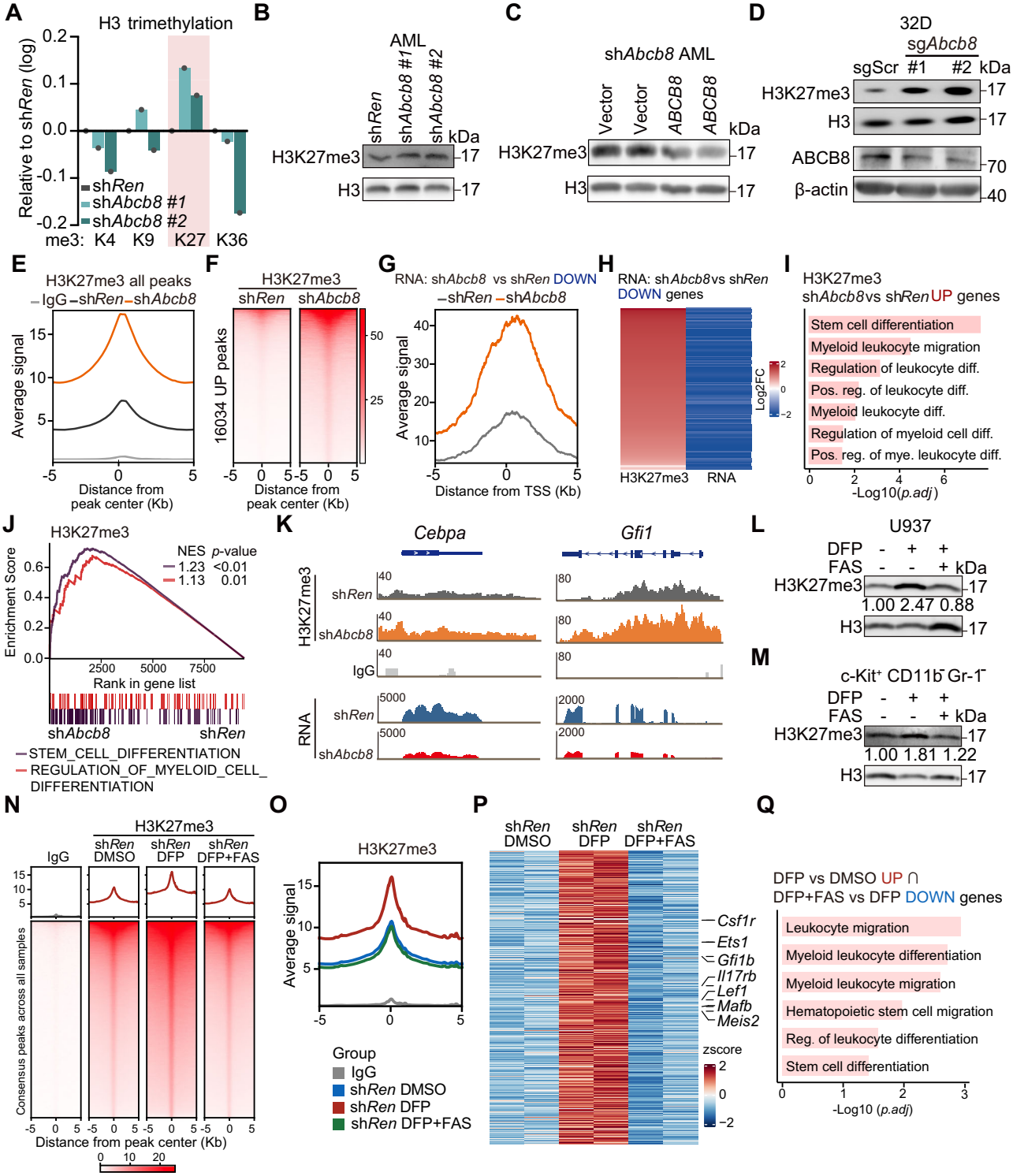


Fig. 3 | ABCB8 promotes differentiation in an iron-dependent manner. **A** FerroOrange (Fe^{2+} probe) staining in sgScr or sg*ABCB8* HL-60 cells. Scale bar, 5 μm. **B** Spatial profiles of FerroOrange (bottom) and DAPI (top) intensities along the transcellular path (white line in 3A). X-axis, distance from line start (pixels). **C** Quantification of nuclear Fe^{2+} levels by FerroOrange mean fluorescence intensity (MFI) in sgScr ($n = 14$), sg*ABCB8*#1 ($n = 59$), or sg*ABCB8*#2 ($n = 43$) HL-60 cells (same n in (**A**–**C**)). **D** Schematic of mitochondrial/nuclear protein extraction and non-heme iron measurement by ferrozine assay. Created in BioRender. Pang, X. (2026) https://BioRender.com/185na5c. **E** The quantification of non-heme Fe^{2+} content in mitochondrial and nuclear proteins in sgScr or sg*ABCB8* HL-60 (left) or MOLM-13 cells (right) ($n = 3$ biological repeats). **F** The percentages of c-Kit$^+$ and Gr-1$^+$ in sh*Abcb8* or sh*Ren* c-Kit$^+$ BM cells, after treatment with DMSO, 40 μM FAS, or 40 μM FAS + 120 μM DFP ($n = 3$ biological repeats). **G** GO enrichment analysis of FAS-upregulated pathways in *Abcb8*-deficient c-Kit$^+$ BM cells. ($p.adj < 0.05$, $n = 3$ biological repeats). **H** GSEA of sh*Abcb8*_vs_sh*Ren*_DN 400 (top 400) gene set in sh*Abcb8*_Veh and sh*Abcb8*_FAS of c-Kit$^+$ BM cells ($n = 3$ biological repeats). **I** Heatmap showing expression patterns of core enrichment genes from Fig. 3H across sh*Ren* or sh*Abcb8* treated with vehicle or FAS-treated c-Kit$^+$ BM cells ($n = 3$ biological repeats). **J** The percentage of c-Kit$^+$ (left) and Gr-1$^+$ (right) in sh*Abcb8* #1 AML with or without *ABCB8* overexpression treated with DMSO or Deferiprone (DFP) after 48 h ($n = 3$ biological repeats). ns (not significant), $^*p < 0.05$, $^{**}p < 0.01$, $^{***}p < 0.001$, $^{****}p < 0.0001$. Data are presented as mean ± SEM (**C**) or mean ± SD (**E**, **F**, **J**). Statistical significance was assessed by two-tailed one-way ANOVA with Dunnett's test (**C**, **E**), two-tailed two-way ANOVA with Šídák's test (**F**), one-sided hypergeometric test with Benjamini-Hochberg adjustment (**G**), permutation-based method in GSEA (**H**) or Fisher's LSD test (**J**). Source data are provided as a source data file.

Specifically, myeloid differentiation genes are significantly enriched among genes bound by KDM6A (including *Cebpa* and *Gfi1*), whereas no such enrichment is observed for those not bound by it (Fig. 5B, C)[34–37]. Furthermore, from the RNA-seq analysis, the heatmap shows that the genes downregulated by *Kdm6a* KO in BM[38] were dramatically and significantly decreased in sh*Abcb8* c-Kit$^+$ HSPCs compared to sh*Ren* cells, which can be reversed by FAS treatment (Fig. 5D, Supplementary Data 3). Among these genes, GO enrichment analysis showed the enrichment of differentiation-related pathways (Supplementary Fig. 5A).

We then explored the role of KDM6A in ABCB8-regulating the HSPC differentiation. We examined KDM6A's impact on the *ABCB8*-overexpressed cells, which can promote sh*Abcb8* AML cell differentiation (Fig. 5E, Supplementary Fig. 5B). In this assay, we found that the effect of ABCB8 in driving cell differentiation was dramatically abolished by sg*Kdm6a*, as shown by increased c-Kit$^+$% and reduced Gr-1$^+$% from flow cytometry analysis (Fig. 5E), and fewer blasts from cytospins images (Fig. 5F). To address whether the demethylase activity of KDM6A is required for *Abcb8*'s tumor-suppressive function, we cloned the wild-type (WT) *KDM6A* and a catalytically inactive, enzyme-dead (ED) *KDM6A* mutant, and investigated their impact on sh*Abcb8* leukemia (Supplementary Fig. 5C, D). sh*Abcb8* leukemia cells developed 2nd leukemia quickly in recipient mice, while exogenous *KDM6A*(WT) but not *KDM6A*(ED) expression significantly inhibited sh*Abcb8* leukemia progression in recipients, as indicated by dramatically reduced GFP$^+$% leukemia cells and blasts in the peripheral blood, and thus extended recipients' survival, KDM6A (ED) exhibited only a



transient inhibitory effect at 2 weeks without survival benefit (Fig. 5G–I). This indicates that KDM6A-mediated tumor suppression primarily depends on its catalytic activity. Altogether, these results support that ABCB8 promotes myeloid differentiation through Fe^{2+}-dependent KDM6A demethylation.

Given that the role of ABCB8 in tumor biology is mainly through KDM6A, we have screened an epigenetic drug library individually to assess its impact on inhibiting sh*Abcb8* leukemia cell growth. Among these, multiple EZH2 inhibitors, including tazemetostat, EI1, etc, exhibited dramatic repression on the sh*Abcb8*-driven AML cell viability compared to wildtype murine c-Kit$^+$ HSPC controls (Fig. 5J, Supplementary Fig. 5E). More tazemetostat-treated, fewer sh*Abcb8* AML cells survived, fewer blasts were observed in cytospin images, and higher differentiation markers CD11b and Gr-1 were expressed (Fig. 5K–M). The trimethylation and acetylation of H3K27 were correspondingly altered with tazemetostat treatment (Fig. 5N). Molecularly, RNA-seq analysis of tazemetostat-treated sh*Abcb8* AML cells confirmed upregulation of myeloid differentiation pathways and associated genes (Fig. 5O, Supplementary Fig. 5F). Corroborating this, GSEA demonstrated that tazemetostat treatment not only upregulated the downregulated genes in sh*Abcb8* c-Kit$^+$ HSPCs (NES = 1.33, *p.adj* < 0.01; Fig. 5P), but also FAS upregulated gene expression signature and KDM6A targets (NES = 1.34,

Fig. 4 | ABCB8 regulates H3K27me3 level. A Bar graphs of histone modification changes in sh*Abcb8* or sh*Ren* AML cells by Western blot (3 independent experiments, see Supplementary Fig. 4A). **B** Western blot of H3K27me3 in sh*Abcb8* or sh*Ren* AML cells (3 independent experiments). **C** Western blot of H3K27me3 in sh*Abcb8* AML cells expressing vector or *ABCB8* cDNA (performed in duplicate wells), representative of three independent experiments. **D** Western blot of H3K27me3 and ABCB8 in 32D cells with sgScr or sg*Abcb8* (3 independent experiments). **E** Average H3K27me3 profile at consensus peaks in sh*Ren* or sh*Abcb8* c-Kit$^+$CD11b$^-$Gr-1$^-$ BM cells, $n = 3$ biological repeats. **F** Heatmap of upregulated H3K27me3 peaks in sh*Abcb8* vs sh*Ren* ($p < 0.05$, $\log_2FC > 1.5$), $n = 3$ biological repeats. **G** H3K27me3 profile at TSS of RNA downregulated genes by sh*Abcb8* vs sh*Ren* ($p < 0.05$, $\log_2FC < -1.5$), $n = 3$ biological repeats. **H** Heatmap of RNA downregulated genes (sh*Abcb8* vs sh*Ren*) with corresponding $\log_2FC$ in RNA and H3K27me3. For H3K27me3, the peak with the highest average signal at each gene's promoter was used, $n = 3$ biological repeats. **I**, **J** GO enrichment analysis (**I**) and GSEA (**J**) of H3K27me3-up pathways in sh*Abcb8* vs sh*Ren* c-Kit$^+$CD11b$^-$Gr-1$^-$ BM cells, using the promoter peak with the highest average signal per gene, $n = 3$ biological repeats. **K** IGV tracks of H3K27me3 and RNA at *Cebpa* and *Gfi1* loci, $n = 3$ biological repeats. **L, M** Western blot of H3K27me3 in U937 (**L**) and c-Kit$^+$CD11b$^-$Gr-1$^-$ BM cells (**M**) treated with DMSO, DFP (150 μM), or DFP (150 μM) + FAS (50 μM) (3 independent experiments). **N** Heatmap showing H3K27me3 at consensus peaks in mouse c-Kit$^+$CD11b$^-$Gr-1$^-$ BM cells treated with DMSO, DFP or DFP and FAS. **O** Average H3K27me3 profiles at consensus peaks (as in N). **P** Heatmap of H3K27me3 CUT&Tag signals at peaks up in DFP vs DMSO and down in DFP + FAS vs DFP, with myeloid differentiation genes highlighted. **Q** GO analysis of genes with H3K27me3 up in DFP (vs. DMSO) and down in DFP + FAS (vs. DFP). (**N**–**Q**, $n = 2$ biological repeats). Statistical significance was assessed by the Wald test in DESeq2 (**F**–**H**), one-sided hypergeometric test with Benjamini-Hochberg adjustment (**I**, **Q**), and permutation-based method in GSEA (**J**). For the quantitative comparison shown in (**B**), samples were derived from the same experiment, and blots were processed in parallel. Source data are provided as a source data file.

p.adj < 0.01; NES = 1.37, *p.adj* < 0.01; Fig. 5P). Thus, our work identifies ABCB8 as a critical factor in leukemia maintenance and suggests EZH2 as a potential therapeutic target for −7/del(7q) AMLs.

The co-deletion of *ABCB8* and *KMT2C* cooperatively drives leukemia formation

ABCB8 is on chromosome 7q36, where another tumor suppressor gene *KMT2C* identified in leukemia is located. In most cases, *ABCB8* is co-deleted with *KMT2C* in -7/del(7q) MDS or AML samples (Supplementary Fig. 6A). Furthermore, we have demonstrated that ABCB8 may work through KDM6A, which is in the same COMPASS-like complex with KMT2C[39]. Thus, we investigated whether there is any synergistic effect of *ABCB8* and *KMT2C* deletions on tumorigenesis (Fig. 6A). As Fig. 6B shown, compared to sh*Kmt2c* only, co-knockdown of *Abcb8* and *Kmt2c* promoted leukemia formation in recipient mice with significantly shorter tumor onset (median onset 89 days for sh*Abcb8* #1; median onset 87.5 days for sh*Abcb8* #2; median onset 131 days for control sh*Ren*). Consistently, sh*Abcb8*; sh*Kmt2c* cohort mice developed higher WBC, lower RBC, Hb and PLT counts, compared to control sh*Ren*; sh*Kmt2c* cohort (Supplementary Fig. 6B). Blood smears results and H&E stainings exhibited aggressive leukemia cells (blast) in the peripheral blood and infiltrated into the spleen, liver, and bone marrow (Supplementary Fig. 6C). The mRNA level of *Abcb8* was reduced correspondingly (Supplementary Fig. 6D). sh*Abcb8*; sh*Kmt2c* vs sh*Ren*; sh*Kmt2c* cells were dramatically increased in the harvested bone marrow compared to that in pre-injection, indicating that the *Abcb8*- and *Kmt2c*-deficient cells were more malignant than *Kmt2c*-loss only cells (Fig. 6C). Given that *Abcb8* or *Kmt2c* loss alone could block HSPCs differentiation, we investigated the impact of the co-repression of *Abcb8* and *Kmt2c* in HSPCs stemness and differentiation, and found that sh*Abcb8*; sh*Kmt2c* synergistically increased c-Kit% (Fig. 6D). Agreeing with this, we found that ABCB8 and KMT2C cooperatively regulate gene expression, especially for genes involved in differentiation-related pathways like myeloid cell differentiation, by transcriptomic analysis of murine c-Kit$^+$ HSPCs transduced with sh*Ren*, sh*Abcb8*, sh*Kmt2c*, or sh*Abcb8*; sh*Kmt2c* (Fig. 6E–G, Supplementary Data 3). Some genes are mainly regulated by *Abcb8*, and some genes are mainly under the control of *Kmt2c*, but many other genes are downregulated by both *Abcb8* and *Kmt2c* loss. Consistently, we observed synergistic effects on the H3K27me3 signal of these genes regulated by both *Abcb8* and *Kmt2c* from murine c-Kit$^+$ HSPCs CUT&Tag data (Fig. 6H). Collectively, these results demonstrate that ABCB8-regulated intracellular iron levels are critical for −7/del(7q) AML cells maintenance.

The role of the ABCB8-Fe^{2+}-KDM6A axis in human −7/del(7q) AML

We also validated our findings of ABCB8 regulating H3K27me3 level through Fe^{2+}-KDM6A in human AML patients. First, we compared the level of H3K27me3 in *ABCB8* high vs low expression AML patients[40], and found that H3K27me3 levels were negatively associated with *ABCB8* expression (Fig. 7A, Supplementary Fig. 7A). We further validated that ABCB8 could regulate H3K27me3 levels through monitoring H3K27me3 in human leukemia HL-60 cells carrying sg*ABCB8* with or without *ABCB8* cDNA. *ABCB8* deficiency by sg*ABCB8* caused an upregulation of H3K27me3, which was repressed when combined with *ABCB8* cDNA (Fig. 7B). Consistent with this, *ABCB8* levels are positively correlated with the expression level of KDM6A binding genes[41] in AML patients from the Beat AML cohort[25] and GSE67040 cohort (Fig. 7C, D, Supplementary Data 5).

We evaluated the dependence of human -7/del(7q) AML cells on *ABCB8*. We found that human AML cell lines with chromosome 7 deletions (UoCM1 and SCU-1) were sensitive to exogenous *ABCB8* expression, while control cell lines (HL-60 and U937) were largely unaffected (Fig. 7E, F). Consistent with this, FAS supplementation reduced the viability of -7/del(7q) AML cells (Fig. 7G).

Having previously shown that *Abcb8*-deficient leukemia cells are sensitive to the EZH2 inhibitor tazemetostat, we next examined the effect of tazemetostat on −7/del(7q) AMLs. In a UoCM1 cell line-derived xenograft (CDX) model, tazemetostat treatment reduced tumor burden, as indicated by significantly lower spleen weight and a reduced percentage of human CD45$^+$ leukemia cells in the bone marrow (Fig. 7H). Blood smear analysis also exhibited more differentiated cells in the tazemetostat-treated cohort (Fig. 7I). Notably, we collected the fresh peripheral blood mononuclear cells (PBMCs) from AML patients (West China Hospital) and treated them with tazemetostat in vitro for 48 h. PBMCs from −7/del(7q) AML patients showed significantly lower viability compared to those from other AML subtypes (Fig. 7J).

In summary, we identified *ABCB8* as a tumor suppressor gene on chromosome 7. Its loss inhibits HSPC differentiation and promotes acute myeloid leukemia formation, likely via the Fe-KDM6A axis, and acts cooperatively with another chromosome 7 tumor suppressor gene, *KMT2C* (Fig. 7K).

Discussion

Chromosome copy number alterations are a hallmark of cancer, which are often associated with poor prognosis. Complete or partial chromosome 7 loss, generally containing hundreds to thousands of genes, has long been recognized as a poor-prognosis biomarker for myeloid malignancies. However, only a few of the chromosome 7 genes, like *KMT2C*[16], *SAMD9*/*SAMD9L*[42], *CUX1*[43], etc, have been demonstrated to play a role in promoting the process of tumor initiation and progression. Here, our studies identified multiple tumor suppressor candidate genes. Among them, we revealed that loss of *ABCB8*, located on 7q36.1, could drive an MDS-like syndrome by itself or AML combined with *TP53* and *NF1* loss in mice. We further illustrated that ABCB8, a transporter participating in the output of mitochondrial iron, affects the

differentiation of hematopoietic stem and progenitor cells into myeloid cells, likely through regulating iron-containing histone methylase KDM6A. These results provide a mechanism of chromosome 7 loss in tumor biology, in which the mitochondrial iron transporter contributes to epigenetic regulation, HSPCs differentiation and cell transformation.

In this study, we illustrated a cellular pathway through which a mitochondrial iron transporter, ABCB8, regulates the epigenetic modification, histone H3 lysine 27 tri-methylation. As we know, the dysfunction of mitochondrial metabolic enzymes IDH1/2 affects DNA methylation levels through TET family proteins. IDH1/2 mutants produce a new metabolite, 2-hydroxyglutarate, which can bind to and inhibit the enzymatic activity of DNA demethylase TET. Here, we reported another way that mitochondrial function plays a role in regulating histone methylation through Fe^{2+} homeostasis and KDM6A, using Fe^{2+} as a cofactor to accomplish the histone demethylase activity.

https://doi.org/10.1038/s41467-026-75292-2

Fig. 5 | *Abcb8* loss affects iron-dependent KDM6A. A, **B** Among genes with increased H3K27me3 in sh*Abcb8* c-Kit$^+$ BM cells (vs. sh*Ren*), KDM6A-bound genes[34] show biased RNA changes (**A**) and enrich myeloid differentiation pathways (**B**). **C** IGV tracks of KDM6A peaks[34,37] on *Cebpa* and *Gfi1* loci in mouse HSPCs. **D**, Heatmap of genes downregulated in *Kdm6a*-KO[38] across sh*Ren*_Veh, sh*Abcb8*_Veh or sh*Abcb8*_FAS c-Kit$^+$ BM cells. Myeloid differentiation genes are highlighted, $n = 3$ biological repeats. **E** Percentages of c-Kit$^+$and Gr1$^+$ in sgScr or sg*Kdm6a* transduced sh*Abcb8* AML cells with or without *ABCB8* overexpression. **F** Wright-Giemsa staining of cells from E ($n = 3$ biological repeats, red arrows indicate differentiated cells). Scale bar, 10 μm. **G**, **H** Percentage of GFP$^+$ cells in peripheral blood (**G**) and representative Wright-Giemsa-stained images (**H**) from Vector, *KDM6A* WT, or *KDM6A* ED cohort at 2 weeks post-transplantation ($n = 6$ mice). Scale bar, 10 μm. **I** Kaplan-Meier AML-free survival of secondary recipient mice. Median survival, Vector, $n = 5$ mice, 12 days; *KDM6A* WT, $n = 8$ mice, not reached; *KDM6A* ED, $n = 6$ mice, 17 days, log-rank test. **J** Viability of sh*Abcb8* AML versus WT c-Kit$^+$ BM cells after 72 h epigenetic drug treatment (3 independent experiments). **K** Viability of WT c-Kit$^+$ BM or sh*Abcb8* AML cells treated with tazemetostat for 72 h ($n = 3$ biological repeats). **L**, **M** Wright-Giemsa staining (**L**) and CD11b/Gr-1 MFI (**M**) of sh*Abcb8* AML cells with vehicle or tazemetostat ($n = 3$ biological repeats). Scale bar, 10 μm. **N** Western blot of H3K27me3, H3K27ac in sh*Ren* or sh*Abcb8* AML cells treated with vehicle or tazemetostat after 48 h (3 independent experiments). **O**, **P** GO enrichment analysis (**O**) and GSEA (**P**) of upregulated pathways in tazemetostat-treated sh*Abcb8* AML cells ($n = 3$ biological repeats). ns, not significant $p > 0.05$, $^{**}p < 0.01$, $^{****}p < 0.0001$. Data are presented as mean ± SEM (**G**) or mean ± SD (**E**, **K**, **M**). Statistical significance was assessed by two-tailed one-way ANOVA with Dunnett's test (**G**, **M**), two-tailed two-way ANOVA with Dunnett's test (**K**), two-sided chi-square test (**A**), one-sided hypergeometric test (**B**), one-sided hypergeometric test with Benjamini-Hochberg adjustment (**O**), permutation-based *p*-values with Benjamini-Hochberg adjustment (**P**). **F**, **H** and **L** are representative images of 6 mice each. For the quantitative comparison shown in (**N**), samples were derived from the same experiment, and blots were processed in parallel. Source data are provided as a source data file.

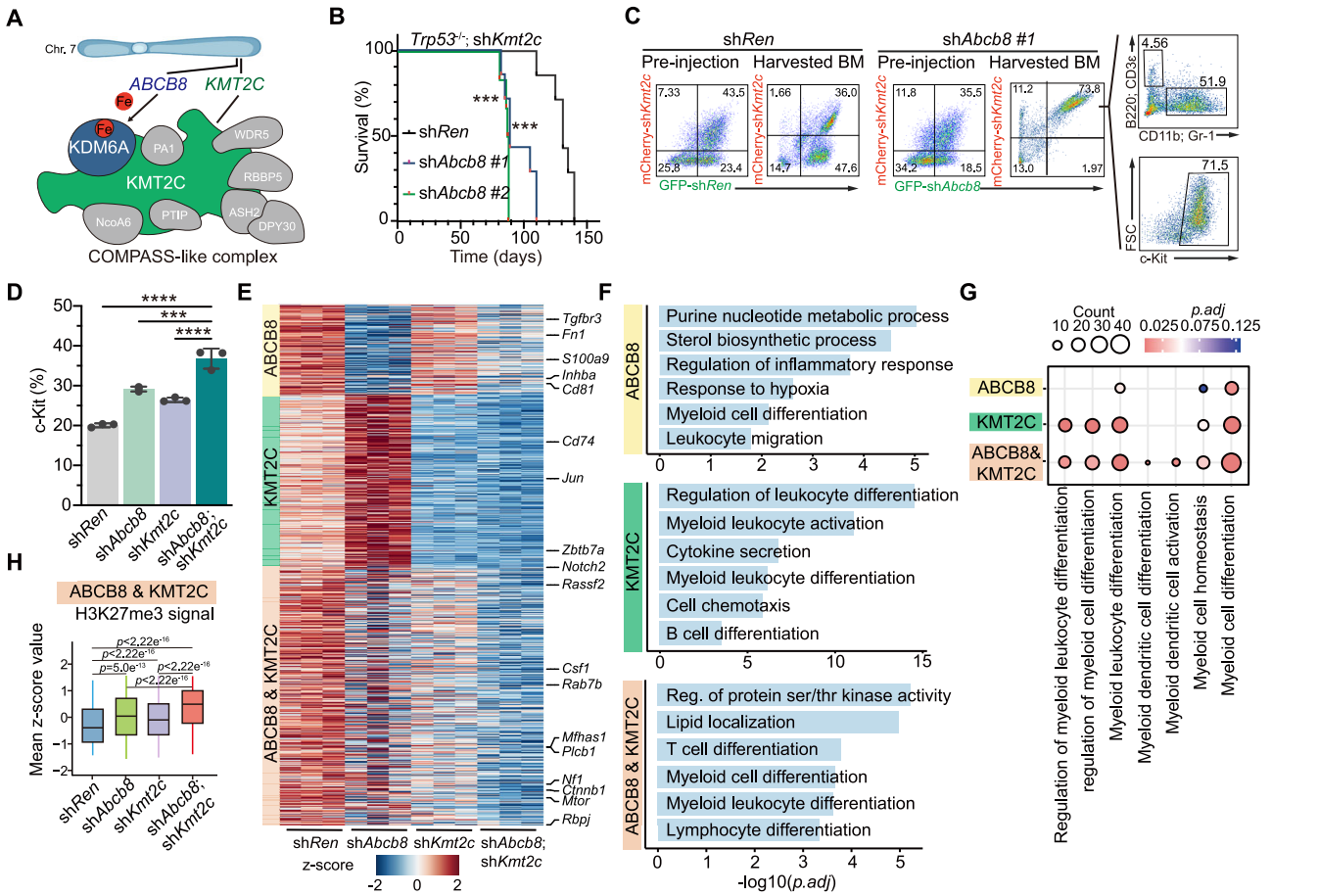


Fig. 6 | *Abcb8* deletion cooperates with *Kmt2c* loss in driving AML. A Schematic diagram of the potential synergistic effect of *ABCB8* and *KMT2C* deletions in 7q deletion-driven tumorigenesis. Created in BioRender. Pang, X. (2026) https://BioRender.com/185na5c. **B** Kaplan-Meier survival curves of recipient mice in vector (sh*Ren*, $n = 7$ mice), sh*Abcb8* #1($n = 6$ mice) or sh*Abcb8* #2 ($n = 7$ mice) cohort, $^{***}p < 0.001$, log-rank test. **C** Flow cytometry of pre-transplant donor cells and recipient BM leukemia cells in sh*Ren* or sh*Abcb8* cohort. **D** The percentage of c-Kit$^+$ cells in sh*Ren*, sh*Abcb8*, sh*Kmt2c*, or sh*Abcb8*; sh*Kmt2c* c-Kit$^+$ BM cells (mean ± SD, $n = 3$ independent cell cultures, $^{***}p < 0.001$, $^{****}p < 0.0001$). **E** Heatmap of union downregulated genes ($\log_2$FC < 0, $p < 0.05$) in sh*Abcb8*, sh*Kmt2c*, and sh*Abcb8*; sh*Kmt2c* mouse c-Kit$^+$ BM cells compared to sh*Ren*, categorized as ABCB8-only, KMT2C-only, or ABCB8 & KMT2C co-regulated ($n = 3$ biological repeats). **F** GO analysis of the three gene sets ($n = 3$ biological repeats). **G** GO analysis of myeloid differentiation-related pathways of the three gene sets ($n = 3$ biological repeats). **H** H3K27me3 CUT&Tag signals at genes downregulated in sh*Abcb8*; sh*Kmt2c* vs sh*Ren* (c-Kit$^+$ BM cells) across sh*Ren*, sh*Abcb8*, sh*Kmt2c*, and sh*Abcb8*; sh*Kmt2c* groups ($n = 3$ independent cell cultures). The center line indicates the median, the box bounds indicate the 25th and 75th percentiles, and the whiskers extend to the smallest and largest observations within 1.5 × IQR from the hinges. Statistical significance was assessed by two-tailed one-way ANOVA with Dunnett's test (**D**), Wald test in DESeq2 (**E**), one-sided hypergeometric test with Benjamini-Hochberg adjustment (**F**, **G**) or two-sided paired Wilcoxon test (**H**). Results in (**C**) are representative images from two independent experiments, $n = 5$ mice. Source data are provided as a source data file.

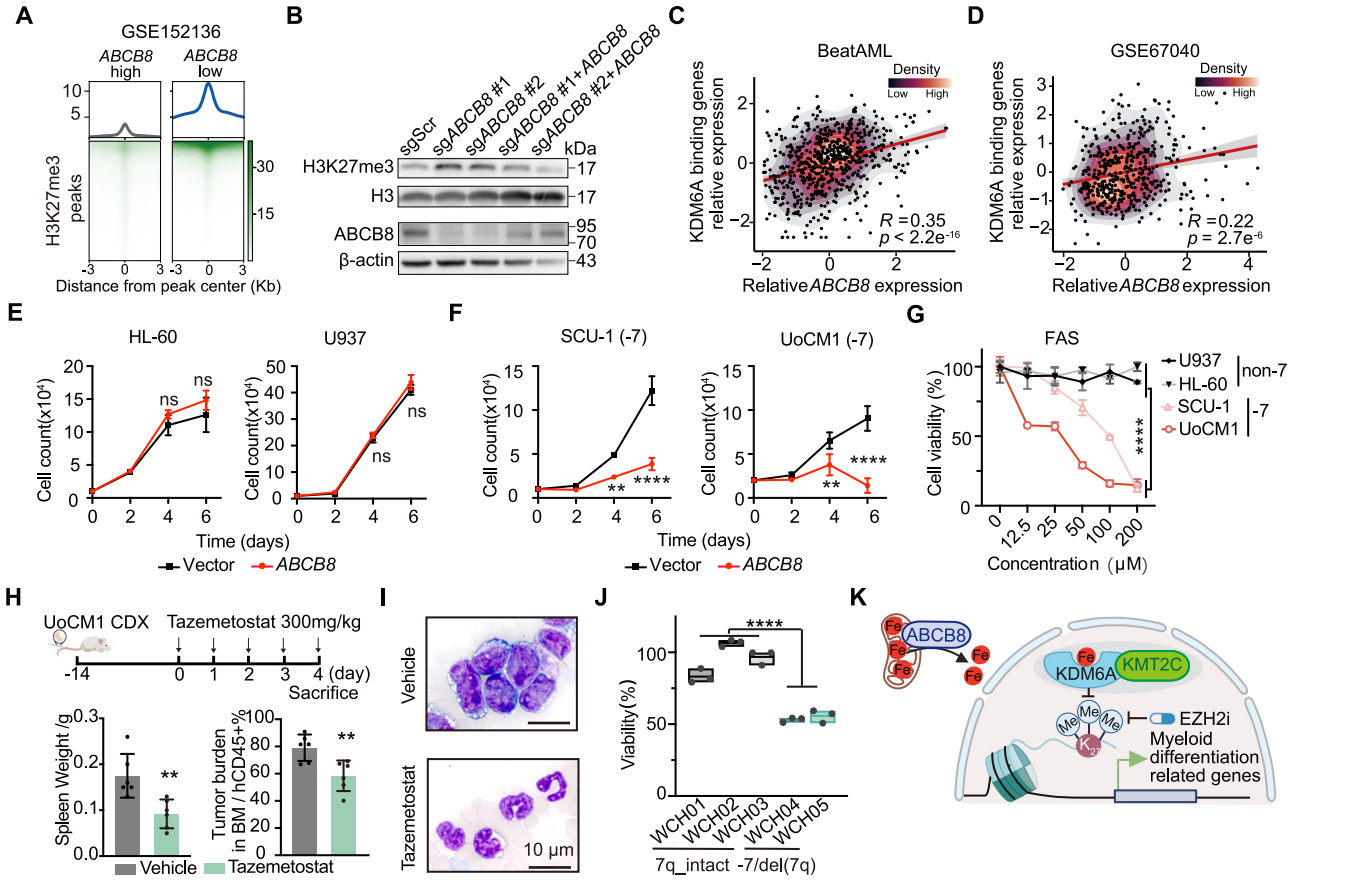


Fig. 7 | The role of the ABCB8-Fe^{2+}-KDM6A axis in human −7/del(7q) AML. **A** Heatmap of H3K27me3 CUT&Tag signal at consensus peaks in AML samples[40], stratified into *ABCB8*-high and -low expression groups ($n = 3$ patients). **B** Protein levels of H3K27me3, ABCB8 in HL-60 with vector only, sg*ABCB8*, or sg*ABCB8* + *ABCB8* overexpression (3 independent experiments). **C**, **D** Scatter plot of correlation between z-scored *ABCB8* expression and KDM6A binding signature[41] in BeatAML[25] (**C**, R = 0.35, p <2.2e^{-16}, $n = 649$) and GSE67040 (D, R = 0.22, $p = 2.7e^{-6}$, $n = 452$) AML patient cohorts. **E**, **F** Growth curves of *ABCB8*-overexpressing versus control in human AML lines with intact (**E**, HL-60, U937) or deleted (**F**, SCU-1, UoCM1) chromosome 7 ($n = 3$ biological repeats). **G** Cell viability of intact (U937, HL-60) versus deleted (SCU-1, UoCM1) chromosome 7 AML cell lines following FAS treatment ($n = 3$ biological repeats). **H** Upper: schematic of CDX model using UoCM1 cells. Created in BioRender. Pang, X. (2026) https://BioRender.com/185na5c. Lower: spleen weight and BM hCD45^{+}% in vehicle or tazemetostat-treated cohort, $n = 6$ mice. **I** Giemsa-stained peripheral blood in vehicle or tazemetostat-treated cohort, representative images from two independent experiments, $n = 6$ mice. Scale bar, 10 μm. **J** Cell viability of 7q-intact (WCH01, WCH02, WCH03) or −7/del(7q) AML (WCH04, WCH05) AML patients after 48 h tazemetostat treatment ($n = 3$ biological repeats). **K** Schematic of ABCB8, KMT2C, KDM6A collaboration and the mechanisms of EZH2 inhibitors in −7/del(7q) leukemia. Created in BioRender. Pang, X. (2026) https://BioRender.com/185na5c. ns (not significant), $^{*}p < 0.05$, $^{**}p < 0.01$, $^{****}p < 0.0001$. Data are presented as mean ± SD (**E**–**H**, **J**). For (**C**, **D**), shaded bands indicate the 95% confidence intervals around the linear regression fits. Statistical significance was assessed by two-sided Spearman's rank correlation test (**C**, **D**), two-tailed one-way ANOVA with Dunnett's test (**E**–**G**, **J**) or two-tailed unpaired t-test (**H**). Source data are provided as a source data file. For the quantitative comparison shown in (**B**), samples were derived from the same experiment, and blots were processed in parallel.

ABCB8 deficiency, causing the defect of iron output from mitochondria, reduced the nuclear iron level, affected histone demethylase function, and related histone H3K27 methylation level. Our findings would expand the understanding of the molecular mechanisms by which mitochondria function to influence epigenetic regulation.

Interestingly, we found the cooperation of *ABCB8* and *KMT2C*, both of which are located on chromosome 7q36. In the frequently deleted chromosomal fragments, it has been reported that multiple tumor suppressor genes are enriched in this region. Moreover, the cooperation among these TSGs was identified before. In most cases, this cooperation is generally cooperative among different cellular pathways, like epigenetic factors PHF23 with transcription factor p53. It is more likely that genes co-deleted with the chromosome deletions promote tumorigenesis through multiple cellular pathways. However, our finding is that the co-deletion of *ABCB8* and *KMT2C* in -7/del(7q) AML affects the same COMPASS-like complex, which may fine-tune this complex function on regulating transcriptomics and have a synergic effect on driving tumor formation.

Methods

Ethics statement

For studies involving human AML samples described below, ethics approval was provided by the Ethical Research Committee on Biomedical Research, West China Hospital of Sichuan University (No.HX-2019-(114)). All participants provided written informed consent prior to participating in the study.

For studies involving mice described below, all animal procedures were approved by the Institutional Animal Care and Use Committee (IACUC) of West China Hospital. Because this study employed leukemia models in which solid tumor volume is not applicable, a specific maximal tumor size/burden was not defined in the approved protocol. Animals were monitored daily for humane endpoints predefined by the ethics committee (e.g., >20% body weight loss, hind-limb paralysis, moribund state). All animals were euthanized by cervical dislocation after anesthesia when reaching the experimental endpoint, without exceeding the maximal tumor burden as defined by the ethics committee.

Human specimens

AML samples were obtained from West China Hospital of Sichuan University, with recruitment conducted between 2021 and 2022, including 2 with −7/del(7q), and 3 with intact 7q. Chromosome 7 status was confirmed by karyotype analysis. Following transport at 4 °C, bone marrow samples were processed to isolate tumor cells from Bone Marrow Mononuclear Cells (BMMCs) using Ficoll-Paque PLUS density gradient centrifugation. All patients were pathologically diagnosed with AML by pathologists at West China Hospital. As the information on sex or gender was not relevant in this study, no related analysis was carried out.

Mice

Trp53$^{-/-}$ mice from The Jackson Laboratory (Stock No: 002101, RRID: IMSR_JAX:002101) and *Trp53*$^{-/-}$; Cas9-expressing mice obtained by breeding *Trp53*$^{-/-}$ mice with Cas9 knock-in mice from The Jackson Laboratory (Stock No: 026179, RRID: IMSR_JAX:026179) served as donor mice (both in C57BL/6 background). Male and female C57BL/6 mice (6-8 weeks old, 20–25 g) were obtained from GemPharmatech Co., Ltd. (Nanjing, China). Both male and female mice were used, as this study did not consider sex as a biological variable. NOD.Cg-Prkdcscid Il2rgtm1/Bcgen (NSG) mice were obtained from Beijing HuaFukang Biological Technology Co., Ltd. All transplantation experiments were conducted when recipient mice were 6-8 weeks of age. All mice were maintained in a temperature-controlled facility with 12 h light/dark cycle at 23 ± 2 °C and 30–70% humidity. Bone marrow cells were freshly isolated from femurs and tibias of male 6 to 8-week-old donor mice, and c-Kit$^+$ HSPCs were sorted using c-Kit (CD117) Microbeads (Miltenyi Biotec Cat# 130-091-224, RRID: AB_2753213) and a QuadroMACS separator (Miltenyi Biotec, South San Francisco, CA). To isolate the c-Kit$^+$ CD11b$^-$Gr-1$^-$ HSPC population, this enriched fraction was subsequently incubated with biotinylated anti-CD11b (Cat# 101203, RRID: AB_312786; BioLegend) and anti-Gr-1 antibodies (Cat# 108403, RRID: AB_313368; BioLegend), followed by the depletion of CD11b$^+$ and Gr-1$^+$ cells via negative selection using Anti-Biotin MicroBeads (Cat# 130-090-485, RRID: AB_244365; Miltenyi Biotec). For sg*Abcb8* in vivo tumorigenesis, *Trp53*$^{-/-}$; *Cas9*$^{+/-}$ c-Kit$^+$ BM cells were co-infected with GFP-linked shRNA and mCherry-linked sgRNA; for sh*Abcb8* in vivo tumorigenesis, *Trp53*$^{-/-}$; c-Kit$^+$ BM cells were co-infected with GFP-linked sh*Abcb8*/sh*Ren* and mCherry-linked sh*Nf1*; then 1×10^6 infected c-Kit$^+$ BM cells were injected into 5.5 Gy irradiated male C57BL/6 recipient mice via the tail vein injection. Investigators were blinded to group assignments during transplantation and outcome assessment. All recipient mice were randomly divided into groups before transplantation and monitored using complete blood count (CBC) and blood smears. Blood count measurement was performed on a Hema-Vet 950FS Blood Analyzer (RRID: SCR_020016). For secondary transplant experiments, 1×10^6 bone marrow leukemia cells were injected into 4.5 Gy irradiated C57BL/6 recipient mice.

Plasmid construction

All newly generated plasmids and cell lines described in this study are available from the corresponding author upon reasonable request.

1) shRNA construction

   Gene-specific shRNA oligonucleotides (97 bp) were designed using splashRNA (http://splashrna.mskcc.org/) and synthesized by Tsingke Biotechnology (Beijing, China). shRNA sequences are listed in Supplementary Data 2; *Kmt2c* shRNA sequences were from a previous report[16]. Complementary oligonucleotides were annealed and cloned into *Eco*RI-HF/*Xho*I-digested retroviral vectors MSCV-shRNA-SV40-GFP, MSCV-shRNA-SV40-mCherry, or MSCV-shRNA-PGK-puromycin-IRES-GFP (all vectors were gifts from the Scott W. Lowe laboratory). All constructs were verified by Sanger sequencing.

2) Genome editing

   sgRNAs were designed using the ATUM CRISPR gRNA Design tool, and corresponding oligonucleotides were synthesized by Tsingke Biotechnology. sgRNA sequences are provided in Supplementary Data 2. To generate the sgRNA expression vector V2TC (U6-sgRNA-EFS-NS-mCherry), the spCas9 coding sequence in V2T (LentiCRISPR v2, Addgene #52961) was replaced with mCherry. Oligonucleotides were annealed and cloned into the *Bsm*BI site of V2TC. The V2T plasmid (expressing Cas9 and puromycin resistance) was used to establish Cas9-expressing cells. To establish sg*ABCB8* HL-60 cell lines, cells were transduced with V2T, selected with puromycin (1 μg m/L, Cat# A1113803, Thermo Fisher Scientific), and subsequently transduced with lentivirus carrying the sgRNA. Mutations were validated by T7E1 assay (Cat# EN303-01, Vazyme, Nanjing, China) using the primers listed in Supplementary Data 2.

3) cDNA cloning

   The human ABCB8 coding sequence was synthesized by Tsingke Biotechnology and cloned into the *Eco*RI-HF/*Xho*I sites of the retroviral vector pMSCV-cDNA-IRES-GFP (a gift from the Scott W. Lowe laboratory). The construct was confirmed by Sanger sequencing.

   All newly generated plasmids (shRNA, sgRNA, and *ABCB8* expression constructs) are available from the corresponding author upon reasonable request.

Flow cytometry

Flow cytometry analyses were performed on the BD LSRFortessa Flow Cytometer (BD Biosciences, San Jose, CA). Surface staining was performed at 4 °C for 30 min using the following antibodies: B220 (BioLegend, 103212, clone RA3-6B2, 1:200), CD3ε (BioLegend, 100312, clone 145-2C11, 1:200), CD11b (BioLegend, 101224, clone M1/70, 1:200), Gr-1 (BioLegend, 108430, clone RB6-8C5, 1:200), c-Kit (BioLegend, 105814, clone 2B8, 1:200), Sca-1 (BioLegend, 108113, clone D7, 1:200), CD48 (BioLegend, 103427, clone HM48-1, 1:200), CD150 (BioLegend, 115927, clone TC15-12F12.2, 1:200), and CD45.1 (BioLegend, 110713, clone A20, 1:200). Data were analyzed using FlowJo software (RRID: SCR_008520). Data were analyzed using FlowJo software V10.0 (RRID: SCR_008520). The gating strategies were defined as follows: LSK (Lin$^-$ Sca-1$^+$ c-Kit$^+$), CMP (Lin$^-$ Sca-1$^-$ c-Kit$^+$ CD34$^+$ CD16/32$^-$), GMP (Lin$^-$ Sca-1$^-$ c-Kit$^+$ CD34$^+$ CD16/32$^+$), MEP (Lin$^-$ Sca-1$^-$ c-Kit$^+$ CD34$^-$ CD16/32$^-$), macrophage (CD11b$^+$), and granocyte (Gr-1$^+$). Additionally, long-term hematopoietic stem cells (LT-HSC, Lin$^-$ Sca1$^+$ c-Kit$^+$ CD48$^-$ CD150$^+$), short-term hematopoietic stem cells (ST-HSC, Lin$^-$ Sca1$^+$ c-Kit$^+$ CD48$^+$ CD150$^+$), and multipotent progenitors (MPP, Lin$^-$ Sca1$^+$ c-Kit$^+$ CD48$^+$ CD150$^-$) were gated on LSK. Antibodies used are displayed in Supplementary Data 6.

Cell line culture

Cell lines were authenticated by STR profiling and tested monthly for mycoplasma contamination. HEK293T (RRID: CVCL_0063) were from ATCC and cultured at 37 °C with 5% CO_2 in Dulbecco's modified Eagle medium (DMEM) supplemented with 10% vol/vol fetal bovine serum (FBS) and penicillin (100 U/mL)/streptomycin (0.1 mg/mL). MOLM-13 (RRID: CVCL_2119), HL-60 (RRID: CVCL_0002), NB4 (RRID: CVCL_0005), and UoCM1(RRID: CVCL_A480) were from DSMZ and cultured at 37 °C with 5% CO_2 in RPMI 1640 medium supplemented with 10% FBS and penicillin (100 U/mL)/streptomycin (0.1 mg/mL). Mouse c-Kit$^+$ HSPCs and AML cells were cultured at 37 °C with 7.5% CO_2 in BCM medium [45% IMDM + 45% DMEM + 10% FBS + 50 μM β-mercaptoethanol + penicillin (100 U /mL)/streptomycin (0.1 mg/mL)] supplemented with 10% stem cell medium (SCM) including mIL-3 (10 ng/mL, Cat# 403-ML; R&D Systems), mIL-6 (10 ng/mL, Cat# 406-ML; R&D Systems), and mSCF (50 ng/mL, Cat# 455-MC; R&D Systems).

Immunoblotting

1×10^6 cells were harvested and lysed in 100 μL Laemmli extraction buffer (Nature 227:680–685, 1970) followed by incubation 5–10 min at 95 °C in metal bath. Lysate proteins were separated by 12–15% SDS-polyacrylamide gel electrophoresis and transferred to polyvinylidene fluoride membranes. Histone blotting was done using acid extracts from cells. The primary antibodies used are displayed in Supplementary Data 6. Relative protein gray-scale values were analyzed using ImageJ (RRID: SCR_003070). All uncropped images for the Western blots are available in the Source Data.

H&E and immunofluorescence staining

H&E staining was performed on mouse organ sections. Briefly, organs were fixed overnight in 4% paraformaldehyde, embedded in paraffin, and sectioned at a thickness of 5 μm. Following deparaffinization and rehydration, the sections were stained with hematoxylin and eosin according to a standard protocol. Stained images were acquired using a panoramic MIDI slide scanner (3DHISTECH). For immunofluorescence analysis, first, the cells were stained with the respective live-cell probes. Specifically, FerroGreen (mitochondrial Fe^{2+}) (Dojindo, #M489) and FerroOrange (cellular Fe^{2+}) (Dojindo, #F374) were used. After staining, the cells were deposited onto glass slides using a cytocentrifuge (CytoSpin 4, Thermo Fisher Scientific), then mounted with an anti-fade mounting medium containing DAPI(Beyotime, #P0131). Images were captured using a Zeiss LSM 880 confocal laser scanning microscope equipped with an Airyscan detector (RRID: SCR_0). To spatially profile Fe^{2+} reduction (Fig. 3A, B), we used ImageJ to extract pixel-by-pixel fluorescence along a linear track ROI traversing the cell. Next, to quantify nuclear Fe^{2+} MFI (Fig. 3C), DAPI-stained nuclei were defined as ROIs. All antibodies used in this study are listed in Supplementary Data 6.

Quantitative PCR

Total RNA was extracted with TRIzol Reagent (Cat# 15596026, Thermo Fisher Scientific), and cDNA was reverse transcribed using Hiscript III RT SuperMix for qPCR (Cat# R323-01, Vazyme) following the manufacturer's instructions. RT-qPCR was performed using ChamQ Universal SYBR qPCR Master Mix (Cat# Q711-02, Vazyme) on the QuantStudio 3 Real-Time PCR System (RRID: SCR_018712). The relative expression of genes was calculated using the 2^−ΔΔct method. Gene expression was normalized to that of *Actb* or *Hprt*. RT-qPCR was performed on each sample in triplicate. Primer sequences used to amplify *Abcb8* were listed in Supplementary Data 2.

In vitro drug response assays

Primary leukemia cells were isolated from sh*Abcb8* tumor-bearing mice and cultured in BCM medium [45% DMEM, 45% Iscove's modified Dulbecco's medium, 10% FBS, 2 mmol/L glutamine, 50 μM β-mercaptoethanol, penicillin (100 U/mL)/streptomycin (0.1 mg/mL)] and were plated in 96-well plates with a cell density of 10,000 cells per well. The plated cells were treated with the indicated concentrations of epigenetic inhibitors (Selleck) or DMSO (Sigma Aldrich, D8418). CCK8 (MCE, HY-K0301) assay counted the number of living cells.

Nuclear and active mitochondrial extraction

Mitochondrial protein lysates were extracted using the following protocol. Generation of acetyllysine antibodies and affinity enrichment of acetylated peptides[44]. Briefly, cells were harvested and homogenized on ice in mitochondrial isolation buffer (10 mM KCl, 1.5 mM $MgCl_2$, 10 mM Tris-Cl, pH 7.4) supplemented with a protease inhibitor cocktail (Roche, Germany). The homogenate was then centrifuged at 1200 *g* for 10 min at 4 °C to collect the precipitate (unbroken cells and nuclei) for nuclear extraction. The resulting supernatant was subjected to a second centrifugation at 4000 *g* for 20 min at 4 °C to eliminate lysosomes and the endoplasmic reticulum. The mitochondrial pellet was subsequently washed with the isolation buffer and centrifuged at 10,000 *g* for 15 min at 4 °C. The collected mitochondrial precipitate was used for subsequent experiments. The precipitate (unbroken cells and nuclei) was collected and further lysed in mitochondrial isolation buffer on ice for 15 min. The homogenate was then centrifuged at 1200 *g* for 10 min at 4 °C to remove the supernatant. The resulting nuclear precipitate was washed twice in isolation buffer and used for subsequent experiments.

Mitochondrial and nuclear iron assay

First, complete mitochondria and nuclei were extracted using the methods mentioned above. Non-heme iron was measured using the following method[44]. In brief, equal amounts of mitochondrial proteins were mixed with protein precipitation solution (1:1 10% trichloroacetic acid plus 1 mol/L HCl) followed by heating for 1 h at 95 °C to release iron. After centrifugation at 4 °C and 16,000 *g* for 10 min, the supernatant was mixed with an equal volume of chromogen solution (1.5 M sodium acetate, 0.5 mM ferrozine, 0.1% (v/v) thioglycolic acid). Absorbance at 562 nm was measured on a multi-mode microplate reader (BioTek Synergy™ H4).

Histone H3 modification multiplex assay

Total histone proteins were extracted from murine AML cells infected with either sh*Ren* or sh*Abcb8* using the EpiQuik™ Total Histone Extraction Kit (EpiGentek, Cat# OP-0006-100) according to the manufacturer's protocol. To profile histone H3 modifications, approximately 100 ng of the extracted histone proteins per well was analyzed using the EpiQuik™ Histone H3 Modification Multiplex Assay Kit (Colorimetric; EpiGentek, Cat# P-3100), strictly following the manufacturer's instructions.

RNA-seq analysis

After library construction, RNA sequencing was performed by an Illumina NovaSeq 6000 sequencing platform with 150 bp paired-end sequencing. The RNA-seq reads were aligned to the mouse reference genome (mm10) by STAR_2.7.10b. Transcript abundances, significance levels, and differentially expressed genes of mouse cells and patient tissue cells were generated and identified by DESeq2 (v.1.26.0) (RRID: SCR_015687). To minimize potential batch effects, expression matrices were adjusted using the removeBatchEffect function from the limma R package prior to principal component analysis (PCA). The significantly differentially expressed genes in each group were used to perform Kyoto Encyclopedia of Genes and Genomes (KEGG) and Gene Ontology (GO) enrichment analyses with the R package clusterProfiler (v. 3.14.3) (RRID: SCR_016884). GSEA (RRID: SCR_003199) was utilized to identify the significantly enriched pathways by default parameters. Preranked function was performed to clarify the overall transcriptome similarity between samples. Pheatmap (v.1.0.12) (RRID: SCR_016418) was used to visualize differentially expressed genes with z-scores.

scRNA-seq analysis

For scRNA-seq of human bone marrow, we acquired the data from the GEO database under the accession number GSE120446[22]. The output of the cellranger and count matrix were read using the Read10X function from the Seurat package (v. 4.3.0) (RRID: SCR_016341). Then the Seurat pipeline was implemented for downstream analyses. Genes expressed in fewer than three cells were not considered. Cells that had mitochondrial ratios lower than 10%, expressed at least 200 but not more than 6000 genes and gene total counts above 200 were retained for analysis. To integrate all the single cells from different samples for unsupervised clustering, the R package Harmony (v. 0.1.1) (RRID: SCR_022206) was used to reduce the batch effect. After data normalization, the 'vst' mode of the "FindVariableFeatures" function was performed for the top 2500 highly variable genes detection. UMAP was performed for cell dimensionality reduction. R package CytoTRACE (v.

0.3.3) (RRID: SCR_022828) was used to estimate cell differentiation potentials. The differentiation trajectory of myeloid cells was constructed using the R package Slingshot. The boxplots display *ABCB8* expression levels, calculated as pseudo-bulk averages across cell types.

CUT&Tag analysis

H3K27me3 CUT&Tag assays were performed using the NovoNGS CUT&Tag 2.0 High-Sensitivity kit (Novoprotein Scientific, N259-YH01-01A). For samples without spike-in controls, libraries were sequenced on an Illumina NovaSeq 6000 platform with 150-bp paired-end reads. Reads were quality controlled using fastp (RRID: SCR_016962) and aligned to the mouse genome (mm10) using Bowtie2 (RRID: SCR_016368). SAMtools (RRID: SCR_002105) was used to convert SAM files into sorted BAM files. Normalized bigWig files were generated using DeepTools (RRID: SCR_016366) with "--normalizeUsing BPM --binSize 50". Data normalization and differential peak analysis were performed using DESeq2 (RRID: SCR_015687).

For samples containing *E. coli* λ sequences as spike-in controls, libraries were sequenced on an Illumina NovaSeq X Plus platform with 150-bp paired-end reads. Reads were quality controlled using fastp and aligned to the mouse genome (mm10) and the *E. coli* λ spike-in sequence using Bowtie2. Sorted BAM files were generated with SAMtools. A scaling factor for each sample was calculated as 10,000 divided by the number of fragments mapped to the *E. coli* genome. Normalized bigWig files were generated using DeepTools with "--normalizeUsing None --binSize 50 --scaleFactor <scaling factor>". IgG samples were normalized without scaling ("--normalizeUsing None --binSize 50"). For differential peak analysis, 1/scaling factor was provided as the size factor to DESeq2 to standardize counts across samples.

For all H3K27me3 data, peaks were called using MACS3 with "--broad --broad-cutoff 0.1 -q 0.05 -f BAMPE". Peak annotation was performed using ChIPseeker with tssRegion set to (−3000, 3000). Broad peaks were converted into GRangesList objects, and consensus counts were generated. Visualization of the average CUT&Tag profiles was performed using DeepTools and IGV (RRID: SCR_011793). For GSEA of H3K27me3 changes, each gene was represented by the peak with the highest mean signal within its promoter. Genes were then ranked by a metric calculated as the cube of the $\log_2$FC multiplied by the mean signal to prioritize genes with both large changes and high signal. Enrichment analysis was performed using the R package clusterProfiler with default parameters and GO Biological Process gene sets.

To analyze the synergistic effect of *ABCB8* and *KMT2C* on H3K27me3 levels, we first extracted H3K27me3 peaks corresponding to genes showing a synergistic effect at the RNA level. For each gene, the average H3K27me3 signal across all peaks was calculated, followed by row-wise z-score normalization. The normalized values were then used to compute the average H3K27me3 level for each group.

Clinical correlation analysis

Genetic alteration data were obtained from TCGA-LAML via cBioPortal (https://www.cbioportal.org/)[20]. Survival analyses for TCGA-LAML[20], Beat AML[25], GSE146173[26] and GSE37642[27] cohorts were performed using the survminer R package (RRID: SCR_021094). In the TCGA-LAML cohort, patients were classified into 7q-intact and 7q-deletion groups based on the CNV status of 7q genes. BeatAML cohort data were downloaded from https://biodev.github.io/BeatAML2/. For the Beat AML[25], GSE146173[26] and GSE37642[27] cohorts, patients were divided into *ABCB8*-high and *ABCB8*-low groups based on *ABCB8* expression, and the optimal cut-point was determined using the maximally selected rank statistics. For the GSE146173[26] cohort, only primary AML samples were included in the analysis. The correlation between *ABCB8* expression and KDM6A binding signature in the BeatAML cohort was analyzed by Seurat. The default "NormalizeData" method was used to normalize the data.

The Bulk RNA-Seq and H3K27me3 CUT&Tag data of AML patients were acquired from the GEO database under the accession number GSE152136[40]. Raw RNA-seq counts were normalized using DESeq2, and the resulting gene expression levels are provided in Supplementary Data 5. Based on these normalized values, we selected three samples with the highest and three with the lowest *ABCB8* expression among patients with both H3K27me3 and RNA-seq data (the two intermediate samples showed no significant expression differences and were therefore excluded from downstream analysis). For CUT&Tag analysis, we used the peak and normalized bigWig files provided by the authors. A consensus peak set was generated from the six selected samples (three *ABCB8*-high and three *ABCB8*-low) by merging individual peak sets using the reduce function in the GenomicRanges package. To compare H3K27me3 signals between the two groups, we averaged the bigwig files of individual samples within each group using the deepTools bigwigAverage function, generating one representative bigwig file per group. The H3K27me3 signal intensity over the consensus peak regions was then quantified using deepTools computeMatrix and visualized with plotHeatmap.

The Leucegene Project Bulk RNA-Seq dataset of AML patients was obtained from GSE67040. The KDM6A ChIP-Seq data of mouse HSPCs were acquired from the GEO database under the accession number GSE86488[34]. Those peak files were downloaded and annotated using the "annotatePeak" function of ChIPseeker (RRID: SCR_021322). The KDM6A ChIP-Seq data of human OCI-AML2 cells were acquired from the GEO database under the accession number GSE214274[41]. Raw sequencing data were processed identically to the CUT&Tag analysis pipeline, with MACS3 peak calling performed using parameters "-g hs -q 0.05 -f BAMPE".

Statistics & reproducibility

No statistical method was used to predetermine sample size. For in vitro studies, 3–4 independent experiments were performed. For in vivo studies, the sample size per group ranged from 4–11, based on the number of animals that developed tumors, including both male and female mice, which have been shown to be sufficient to detect physiologically relevant differences while maintaining experimental feasibility. All key experiments were repeated independently at least twice with similar results, and sample sizes for each experiment are clearly indicated in the figure legends. No data were excluded from the analyses. Unless otherwise stated, samples were randomly assigned to groups prior to the experiments. Investigators were blinded to group allocation during animal transplantation and outcome assessment. No sex-specific differences were observed. Unless otherwise noted, n represents the number of biological replicates. Statistical analyses were performed using GraphPad Prism (v5.01, RRID: SCR_002798) and PASW Statistics 18 software. Two-tailed Student's *t*-tests were used for comparisons between two groups, while one-way or two-way ANOVA was utilized for single-variable or two-variable comparisons among multiple groups, respectively. Additional statistical methods, including the Wilcoxon signed-rank test, Wald test, hypergeometric distribution, and log-rank test, were applied as appropriate for specific datasets. Exact *P* values are provided in the Source Data file, and statistical significance was defined as $p < 0.05$. Error bars are presented as SD or SEM, as specified in the figure legends.

Reporting summary

Further information on research design is available in the Nature Portfolio Reporting Summary linked to this article.

Data availability

The RNA-seq and CUT&Tag data generated in this study have been deposited in the NCBI Gene Expression Omnibus under accession code

GSE294258. The TCGA-LAML patient cohort RNA-seq and copy-number variation data were obtained from cBioPortal [https://www.cbioportal.org/][20]. The BeatAML cohort RNA-seq data were sourced from [https://biodev.github.io/BeatAML2/][25]. Other publicly available sequencing data used in this study: human bone marrow scRNA-seq data from GSE120446[22]; AML patient RNA-seq data from GSE146173[26]; AML patient RNA-seq data from GSE37642[27]; AML patient RNA-seq and H3K27me3 CUT&Tag data from GSE152136[40]; Leucegene Project AML patient RNA-seq data from GSE67040; mouse HSPC KDM6A ChIP-seq data from GSE141560[37]; mouse HSPC KDM6A ChIP-seq data from GSE86488[34]; human OCI-AML2 KDM6A ChIP-seq data from GSE214274[41]. All data are included in the Source Data file or available from the authors. The remaining data are available within the Article, Supplementary Information or Source Data file. Source data are provided with this paper.

Code availability

The analysis code can be found on GitHub (https://github.com/qihop/ABCB8).

References

1. Hanahan, D. & Weinberg, R. A. Hallmarks of cancer: the next generation. *Cell* **144**, 646–674 (2011).
2. Hanahan, D. Hallmarks of cancer: new dimensions. *Cancer Discov.* **12**, 31–46 (2022).
3. ICGC/TCGA Pan-Cancer Analysis of Whole Genomes Consortium Pan-cancer analysis of whole genomes. *Nature* **578**, 82–93 (2020).
4. Soenen, V. et al. 17p Deletion in acute myeloid leukemia and myelodysplastic syndrome. Analysis of breakpoints and deleted segments by fluorescence in situ. *Blood* **91**, 1008–1015 (1998).
5. Inaba, T., Honda, H. & Matsui, H. The enigma of monosomy 7. *Blood* **131**, 2891–2898 (2018).
6. Baker, T. M., Waise, S., Tarabichi, M. & Van Loo, P. Aneuploidy and complex genomic rearrangements in cancer evolution. *Nat. Cancer* **5**, 228–239 (2024).
7. Liu, Y. et al. Deletions linked to TP53 loss drive cancer through p53-independent mechanisms. *Nature* **531**, 471–475 (2016).
8. Hasle, H. et al. Monosomy 7 and deletion 7q in children and adolescents with acute myeloid leukemia: an international retrospective study. *Blood* **109**, 4641–4647 (2007).
9. Mori, M. et al. Genomics of deletion 7 and 7q in myeloid neoplasm: from pathogenic culprits to potential synthetic lethal therapeutic targets. *Leukemia* **37**, 2082–2093 (2023).
10. Solimini, N. L. et al. Recurrent hemizygous deletions in cancers may optimize proliferative potential. *Science* **337**, 104–109 (2012).
11. Cai, Y. et al. Loss of chromosome 8p governs tumor progression and drug response by altering lipid metabolism. *Cancer Cell* **29**, 751–766 (2016).
12. Tschaharganeh, D. F., Bosbach, B. & Lowe, S. W. Coordinated tumor suppression by chromosome 8p. *Cancer Cell* **29**, 617–619 (2016).
13. TP53 Is Not the Only Driver of Chromosome 17p Loss. *Cancer Discov* **6**, 470, https://doi.org/10.1158/2159-8290.Cd-rw2016-058 (2016).
14. Scuoppo, C. et al. A tumor suppressor network relying on the polyamine-hypusine axis. *Nature* **487**, 244–248 (2012).
15. Chen, M. et al. An epigenetic mechanism underlying chromosome 17p deletion-driven tumorigenesis. *Cancer Discov.* **11**, 194–207 (2021).
16. Chen, C. et al. MLL3 is a haploinsufficient 7q tumor suppressor in acute myeloid leukemia. *Cancer Cell* **25**, 652–665 (2014).
17. Schiffer, C. A., Lee, E. J., Tomiyasu, T., Wiernik, P. H. & Testa, J. R. Prognostic impact of cytogenetic abnormalities in patients with de novo acute nonlymphocytic leukemia. *Blood* **73**, 263–270 (1989).
18. Scherer, S. W. et al. Human chromosome 7: DNA sequence and biology. *Science* **300**, 767–772 (2003).
19. Halik, A. et al. Genomic characterization of AML with aberrations of chromosome 7: a multinational cohort of 519 patients. *J. Hematol. Oncol.* **17**, 70 (2024).
20. Ley, T. J. et al. Genomic and epigenomic landscapes of adult de novo acute myeloid leukemia. *N. Engl. J. Med.* **368**, 2059–2074 (2013).
21. Kotini, A. G. et al. Functional analysis of a chromosomal deletion associated with myelodysplastic syndromes using isogenic human induced pluripotent stem cells. *Nat. Biotechnol.* **33**, 646–655 (2015).
22. Oetjen, K. A. et al. Human bone marrow assessment by single-cell RNA sequencing, mass cytometry, and flow cytometry. *JCI Insight* https://doi.org/10.1172/jci.insight.124928 (2018).
23. Gulati, G. S. et al. Single-cell transcriptional diversity is a hallmark of developmental potential. *Science* **367**, 405–411 (2020).
24. Kassambara, A. et al. Survminer: drawing survival curves using 'ggplot2' v. 0.5.2 (2026).
25. Bottomly, D. et al. Integrative analysis of drug response and clinical outcome in acute myeloid leukemia. *Cancer cell* **40**, 850–864.e859 (2022).
26. Bamopoulos, S. A. et al. Clinical presentation and differential splicing of SRSF2, U2AF1 and SF3B1 mutations in patients with acute myeloid leukemia. *Leukemia* **34**, 2621–2634 (2020).
27. Li, Z. et al. Identification of a 24-gene prognostic signature that improves the European LeukemiaNet risk classification of acute myeloid leukemia: an international collaborative study. *J. Clin. Oncol.* **31**, 1172–1181 (2013).
28. Ichikawa, Y. et al. Disruption of ATP-binding cassette B8 in mice leads to cardiomyopathy through a decrease in mitochondrial iron export. *Proc. Natl. Acad. Sci. USA* **109**, 4152–4157 (2012).
29. Tadokoro, T. et al. Mitochondria-dependent ferroptosis plays a pivotal role in doxorubicin cardiotoxicity. *JCI insight* https://doi.org/10.1172/jci.insight.132747 (2020).
30. Li, F. et al. Procaspase-3-activating compound 1 stabilizes hypoxia-inducible factor 1α and induces DNA damage by sequestering ferrous iron. *Cell Death Dis.* **9**, 1025 (2018).
31. Jiang, Y. et al. Iron-dependent histone 3 lysine 9 demethylation controls B cell proliferation and humoral immune responses. *Nat. Commun.* **10**, 2935 (2019).
32. Chen, Z. et al. Structural insights into histone demethylation by JMJD2 family members. *Cell* **125**, 691–702 (2006).
33. Wartman, L. D. et al. Sequencing a mouse acute promyelocytic leukemia genome reveals genetic events relevant for disease progression. *J. Clin. Investig.* **121**, 1445–1455 (2011).
34. Gozdecka, M. et al. UTX-mediated enhancer and chromatin remodeling suppresses myeloid leukemogenesis through noncatalytic inverse regulation of ETS and GATA programs. *Nat. Genet* **50**, 883–894 (2018).
35. Avellino, R. & Delwel, R. Expression and regulation of C/EBPα in normal myelopoiesis and in malignant transformation. *Blood* **129**, 2083–2091 (2017).
36. Hock, H. et al. Gfi-1 restricts proliferation and preserves functional integrity of hematopoietic stem cells. *Nature* **431**, 1002–1007 (2004).
37. Takano, J. et al. PCGF1-PRC1 links chromatin repression with DNA replication during hematopoietic cell lineage commitment. *Nat. Commun.* **13**, 7159 (2022).
38. Wu, B. et al. Epigenetic drug library screening identified an LSD1 inhibitor to target UTX-deficient cells for differentiation therapy. *Signal Transduct. Target. Ther.* **4**, 11 (2019).
39. Wang, L. & Shilatifard, A. UTX mutations in human cancer. *Cancer cell* **35**, 168–176 (2019).
40. Xu, J. et al. Subtype-specific 3D genome alteration in acute myeloid leukemia. *Nature* **611**, 387–398 (2022).

41. Zhou, X., Zhang, P., Aryal, S., Zhang, L. & Lu, R. UTX loss alters therapeutic responses in KMT2A-rearranged acute myeloid leukemia. *Leukemia* **37**, 226–230 (2023).
42. Nagamachi, A. et al. Haploinsufficiency of SAMD9L, an endosome fusion facilitator, causes myeloid malignancies in mice mimicking human diseases with monosomy 7. *Cancer cell* **24**, 305–317 (2013).
43. McNerney, M. E. et al. CUX1 is a haploinsufficient tumor suppressor gene on chromosome 7 frequently inactivated in acute myeloid leukemia. *Blood* **121**, 975–983 (2013).
44. Rebouche, C. J., Wilcox, C. L. & Widness, J. A. Microanalysis of nonheme iron in animal tissues. *J. Biochem. Biophys. Methods* **58**, 239–251 (2004).

Acknowledgments

We thank all the members of the Chen and Liu laboratory for their invaluable suggestions and technical support. We thank Dr. Yuquan Wei for his generous support. We thank Dr. Rezhan Tong for his technical support. We thank the Core Facilities of West China Hospital for technical support. Some of the results obtained in this publication are based upon data generated by the Leucegene group, primarily located at IRIC in Montreal, Canada and supported by Genome Canada and Genome Québec. This data was made possible through human AML specimens provided by the BCLQ, Montreal, Canada.

Author contributions

Y.Liu, C.C., and J.Z. conceived the project and designed experiments. J.Z., Y.P., X.D., Z.W., L.Zhang, L.Zheng, Q.Z., Y. Li, and Z.Q. performed experiments and analyzed data. Y.P., X.C., and J.Z. performed bioinformatic analyses. H.L., T.N., Lan.W., M.L., Y.W., and W.Z. provided critical research materials and technical support. J.Z., Y.P., X.D., X.C., L.Zhang, Li.W., W.C., Y.Liu, and C.C. contributed to data interpretation and discussion. J.Z., X.D., Z.W., Y.P., L.Zhang, Y.Liu, and C.C. prepared and wrote the manuscript. All authors read and approved the final manuscript.

Funding

Y.L. discloses support for the research of this work from National Science and Technology Major Project of China [grant number 2023ZD0500500], National Natural Science Foundation of China [grant numbers 82130007 and 82470188], Sichuan Science and Technology Program [grant numbers 2025NSFTD0030 and 2023ZYD0057], Frontiers Medical Center, Tianfu Jincheng Laboratory Foundation [grant number 2025ZH030], and 1.3.5 Project for Disciplines of Excellence, West China Hospital, Sichuan University [grant number ZYGD22012]. C.C. discloses support for the research of this work from National Science and Technology Major Project of China [grant number 2024YFF0507400], National Natural Science Foundation of China [grant numbers T2221004, 82330087 and 82170171], Sichuan Science and Technology Program [grant number 2025ZNSFSC0047], Frontiers Medical Center, Tianfu Jincheng Laboratory Foundation [grant number TFJC2023010004], and National Clinical Research Center for Geriatrics, West China Hospital, Sichuan University [grant number Z2024JC001]. J.Z. discloses support for the research of this work from the Post-Doctor Research Project, West China Hospital, Sichuan University [grant number 2024HXBH179]. All other authors declare no relevant funding.

Competing interests

The authors declare no competing interests.

Additional information

Supplementary information The online version contains supplementary material available at https://doi.org/10.1038/s41467-026-75292-2.

Correspondence and requests for materials should be addressed to Chong Chen or Yu Liu.

Peer review information *Nature Communications* thanks the anonymous reviewers for their contribution to the peer review of this work. A peer review file is available.

Reprints and permissions information is available at http://www.nature.com/reprints

Publisher's note Springer Nature remains neutral with regard to jurisdictional claims in published maps and institutional affiliations.Data sharing statementThe RNA-seq and CUT&Tag data in this study are deposited in the NCBI Gene Expression Omnibus under accession number GSE294258.

Open Access This article is licensed under a Creative Commons Attribution-NonCommercial-NoDerivatives 4.0 International License, which permits any non-commercial use, sharing, distribution and reproduction in any medium or format, as long as you give appropriate credit to the original author(s) and the source, provide a link to the Creative Commons licence, and indicate if you modified the licensed material. You do not have permission under this licence to share adapted material derived from this article or parts of it. The images or other third party material in this article are included in the article's Creative Commons licence, unless indicated otherwise in a credit line to the material. If material is not included in the article's Creative Commons licence and your intended use is not permitted by statutory regulation or exceeds the permitted use, you will need to obtain permission directly from the copyright holder. To view a copy of this licence, visit http://creativecommons.org/licenses/by-nc-nd/4.0/.

© The Author(s) 2026